Nanoflows induced by MEMS and NEMS: Limits of two-dimensional models

Alyssa T. Liem, Atakan B. Ari, Chaoyang Ti, Mark J. Cops, James G. McDaniel, and Kamil L. Ekinci

Phys. Rev. Fluids **6**, 024201 — Published 2 February 2021

DOI: 10.1103/PhysRevFluids.6.024201

Nanoflows Induced by MEMS and NEMS: Limits of Two-Dimensional Models

Alyssa T. Liem,[1,*] Atakan B. Ari,[1] Chaoyang Ti,[1] Mark J. Cops,[1] James G. McDaniel,[1] and Kamil L. Ekinci[1,†]

[1] *Department of Mechanical Engineering, Boston University, Boston, Massachusetts 02215, USA*

Here, we study viscous oscillatory nanoflows generated in a fluid by mechanical oscillations of miniaturized resonators. In particular, we focus on the limits of two-dimensional cylinder theory, which approximates a slender nanoresonator, such as an AFM microcantilever or a nano-beam resonator, as a cylinder oscillating in a fluid. The cylinder theory is the mainstay in the micro-/nano-electromechanical systems (MEMS/NEMS) literature, but is only accurate in certain regimes. We observe and explain two distinct routes to the breakdown of the cylinder theory. First, when a substrate is present, squeeze film effects become significant and the cylinder theory under-predicts the fluid force applied to the resonator. Second, the cylinder theory over-predicts the fluid force when axial flow becomes relatively large. This occurs at higher bending modes where the spatial gradients along the beam are larger. A dimensionless squeeze number and axial flow number are introduced to facilitate in-depth investigations into the limitations of the two-dimensional cylinder theory. Results from experiments and three-dimensional finite element models are presented in order to illustrate where two-dimensional flow models break down.

I. INTRODUCTION

In the last few decades, silicon-based miniaturized mechanical devices have been developed for a number of applications and fundamental studies. The microcantilever, first envisioned for sensing surface forces in atomic force microscopy (AFM), has quickly gone beyond AFM and found numerous applications in sensing other physical and biological quantities. More recently, even smaller mechanical devices with sub-micron linear dimensions, called nanoelectromechanical systems (NEMS) [1], have moved to the focus of emerging technologies and fundamental experiments. One typically uses these miniaturized mechanical devices as resonators, actuating the nanomechanical oscillations of a normal mode and tracking the changes in the phase and amplitude of the oscillations due to external perturbations.

Because most applications require operation in viscous fluids [2, 3], with air and water being the two most common, fluid dynamics has been a pillar of MEMS/NEMS research. Fluidic coupling results in energy dissipation and mass loading. In device terms, these represent reductions in the quality factor (Q factor or Q) and the resonance frequency, which are central to determining the operational limits of a resonator. In setting up the fluid dynamics problem, one typically treats the solid resonator as an oscillating boundary with no-slip conditions, which generates an oscillating flow. The flow, in turn, exerts forces on the resonator and results in dissipation and mass loading. The amplitude of the oscillations typically do not exceed a few nanometers — hence, prompting terms such as nanoflows [4] and nanofluidics [5]. Even though the general problem of a solid body oscillating in a viscous fluid was treated by G. G. Stokes in 1851 and others subsequently, it is still relevant in the context of MEMS and NEMS research, with many subtle details requiring further attention.

In this manuscript, our focus is on the fluid dynamics of simple but ubiquitous structures in the MEMS/NEMS domain. Fig. 1a shows such a structure, namely a nanomechanical doubly-clamped beam with linear dimensions of $L \times b \times h \approx 40\ \mu\text{m} \times 950\ \text{nm} \times 93\ \text{nm}$, and a substrate-to-beam gap distance of $g \approx 2\ \mu\text{m}$. A second common geometry is the cantilever beam, which provides a lower spring constant compared to a doubly-clamped beam and is the preferred geometry of scanning probe microscopy (SPM) sensors. In the viscous limit [6], the nanoflows induced by the oscillations of both a doubly-clamped beam and a cantilever are often predicted from a two-dimensional (2D) oscillating cylinder model [7, 8]. With the 2D model, the force applied by the fluid to the resonator is computed from a hydrodynamic function, and upon further analysis the total dissipation and quality factor of the fluid-loaded resonator may be predicted. Due to its simplicity and accuracy in certain regimes, the 2D cylinder approximation has been the mainstay in predicting the response and flows around slender structures, such as a MEMS/NEMS resonator. However, use of the 2D cylinder model requires significant approximations to be made in order to simplify the physical problem, which is in nature three-dimensional (3D).

In this manuscript, we present a comprehensive and quantitative assessment of the accuracy of the 2D cylinder approximation in predicting the response of a MEMS/NEMS resonator immersed in a viscous fluid. Two dimensionless parameters that characterize the resonator and fluid field are introduced to facilitate the assessment and predict

* atliem@bu.edu
† ekinci@bu.edu

regimes in which the 2D approximation is accurate. In particular, the accuracy of the approximation will be examined for two cases. The first case examines a resonator vibrating near a substrate [9–12]. For this case, the presence of a substrate gives rise to squeeze film effects which are not accounted for in the 2D cylinder approximation, as an infinite fluid medium is assumed. The second case examines the effect of axial flow, namely flow along the length of the beam, on the mechanical response of the fluid-loaded resonator. For this case, it is clear that the 2D approximation presents a major limitation, as it only considers the fluid field in the 2D plane that the cylinder oscillates in. Although the presence of axial flow results in additional velocity gradients, and therefore viscous stresses, it is found that axial flow reduces the total dissipation, and consequently increases the Quality factor of the resonator.

In the present work, a dimensionless squeeze number and axial flow number are introduced to examine the limitations of the 2D cylinder approximation with respect to the two cases under examination. The dimensionless squeeze number quantifies the extent to which the substrate affects the fluid field, and thus the fluid loading of the resonator. Previously, Bao et al. [10] introduced a dimensionless number that quantified the degree of gas compression. The dimensionless number introduced by Bao et al. determined when elastic forces presented by the gas would dominate over damping forces. In contrast, the dimensionless squeeze number introduced in the present work quantifies the total effect of the squeeze film, which includes stiffness, damping and inertial forces. In the present work the dimensionless axial flow number predicts when flow along the length of the beam will be significant. The dimensionless axial flow number is similar to the normalized wavenumber presented by Van Eysden et al. [13]. In the present work, the dimensionless axial flow number is computed from the flexural wavenumber for a finite beam with discrete natural frequencies. In contrast, the normalized wavenumber presented by Van Eysden et al. was computed from an arbitrary wavenumber of an infinite beam. The analysis presented by Van Eysden et al. was limited to infinite beams with zero thickness and only considered a single wave traveling along the length of the beam, thus resulting in a significant simplification of a finite 3D beam that has reflected and near-field waves [14]. The two dimensionless parameters formulated and analyzed in the present work differ from previously formulated parameters discussed above, and will be essential when analyzing physical MEMS and NEMS devices and the effects of 3D flow.

In this manuscript, measurements from two NEMS beams, with lengths of 50 μm and 60 μm, vibrating near a substrate in viscous fluids are presented to illustrate the effect of squeeze film damping. The accuracy of the 2D approximation is examined by comparison to measurements, and further quantified with use of numerical 3D Finite Element Models (FEMs). To facilitate the comparison between experimental measurements, numerical simulation results, and analytical predictions from 2D approximations, a succinct modal analysis of a fluid-loaded beam is presented. The analysis is a significant contribution of the present work, as it provides a new means for analyzing the effect of fluid loading via the dynamic stiffness, and the modal stiffness, mass and damping parameters. Additionally, numerical parametric studies are performed with the FEMs to investigate the dependence on the dimensionless squeeze and axial flow numbers. These studies scan relatively large ranges of the dimensionless parameters which have not yet been analyzed in previous works, and provide new findings on how 3D flows induced by the vibration of miniaturized resonators affect the beam's response. Specifically, it is found that the axial flow, and therefore fluid loading, depend on both the dimensionless axial flow number and bending mode number. Furthermore, it is found that the 2D cylinder model breaks down for large dimensionless squeeze and axial flow numbers. In these regimes, a full 3D FEM must be employed to accurately predict the fluid field and response of the fluid-loaded resonator. Physical conditions necessary for neglecting the 3D fluid field are discussed, and approximate ranges on the dimensionless numbers for the aforementioned conditions are presented.

The remainder of this paper is organized as follows. In the following section, a general Fluid-Structure-Interaction (FSI) problem is introduced in preparation for the analysis of a resonator immersed in a viscous fluid. An expression for the fluid loading is found and subsequently used when formulating the equation of motion of a fluid-loaded beam in Sec. III. In Sec. III, analysis that derives the modal equation of motion and modal properties of a fluid-loaded beam is presented. These derived modal expressions are essential and will be used to quantify the accuracy of the 2D cylinder approximation. In Sec. IV, the 2D cylinder approximation is presented, and the hydrodynamic function is introduced. The modal properties predicted by the cylinder approximation and hydrodynamic function are also presented in Sec. IV. In Sec. V, the experimental and numerical methods employed in the paper are presented. Results examining the validity of the 2D cylinder approximation are presented in Sec. VI. The effect of a substrate and axial flow are presented, and the accuracy of the 2D cylinder approximation is inspected by comparing the approximation to experimental and numerical results. In Sec. VI, the dimensionless squeeze number and axial flow number are introduced. Measurements from a NEMS beam vibrating in air and water show that the 2D cylinder model breaks down for large values of the dimensionless squeeze number. These results are supported by results from the 3D numerical models and parametric studies. Additional parametric studies illustrate the dependence of axial flow on beam dimensions and mode number. It is found that an increase in axial flow number, and consequently axial flow, results in the breakdown of the 2D cylinder approximation.

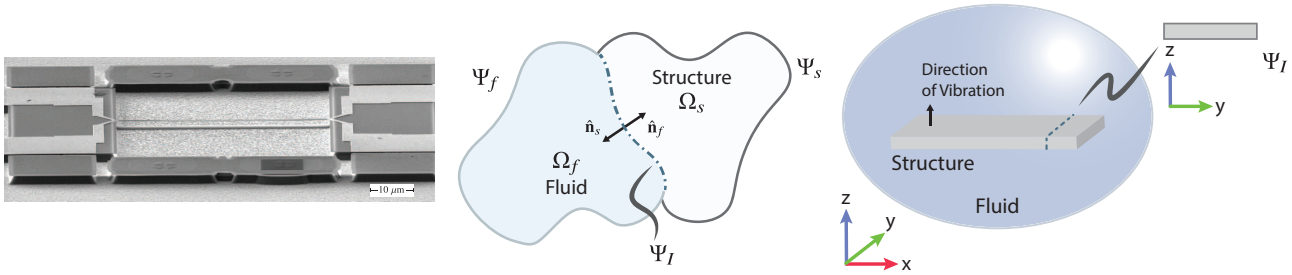

(a) (b) (c)

FIG. 1. (a) Scanning electron microscope image of a nanomechanical beam. Schematic of (b) a general fluid-structure interaction problem and (c) a beam immersed in a fluid.

II. FLUID-STRUCTURE INTERACTION

In this section, the formulation of an FSI problem is discussed, and the problem of a solid MEMS/NEMS resonator immersed in a viscous fluid is introduced. To begin, consider the FSI problem depicted in Fig. 1b. The subscripts f and s denote the fluid and structural quantities. The fluid's domain and boundary are indicated by Ω_f and Ψ_f, respectively, and the structure's domain and boundary are indicated by Ω_s and Ψ_s, respectively. The fluid-structure interface, Ψ_I, is the common boundary of the domains. At the fluid-structure interface Ψ_I, the kinematic boundary condition is [15]

$$\dot{\mathbf{u}}_s = \mathbf{v}_f, \tag{1}$$

where $\mathbf{u}_s$ is the displacement field of the solid, and $\dot{\mathbf{u}}_s$ and $\mathbf{v}_f$ are the velocity fields of the structure and fluid, respectively. Additionally, at the interface Ψ_I, the dynamic boundary condition is

$$-\boldsymbol{\sigma}_s \cdot \hat{\mathbf{n}}_s = \boldsymbol{\sigma}_f \cdot \hat{\mathbf{n}}_f, \tag{2}$$

where $\boldsymbol{\sigma}_s$ and $\boldsymbol{\sigma}_f$ are the total stress tensors of the solid and fluid, respectively, and $\hat{\mathbf{n}}_s$ and $\hat{\mathbf{n}}_f$ are the normal vectors pointing outwards of Ω_s and Ω_f, respectively.

The vectors in Eq. 2 are traction vectors representing the force per unit area acting in the x, y, and z-direction at a given location. Considering the right-hand-side of Eq. 2, the traction vector is

$$\boldsymbol{T} = \begin{Bmatrix} T_x \\ T_y \\ T_z \end{Bmatrix} = \boldsymbol{\sigma}_f \cdot \hat{\mathbf{n}}_f. \tag{3}$$

A 3D resonator immersed in a viscous fluid, as depicted in Fig. 1c, is now considered. For the present work, the resonator is a beam with either doubly-clamped or fixed-free boundary conditions. The beam's length is along the x-axis and the beam vibrates in the z-direction. When the beam vibrates, the stresses in the fluid give rise to forces applied to the beam [16, 17]. Considering a cross-section of the beam in the $y-z$ plane, as depicted in Fig. 1c, the force per unit length applied by the beam to the fluid is found from the boundary integrals taken over the boundary Ψ_I. For example, the force per unit length applied along the beam in the z-direction is

$$\overline{f}_{s|f,z}(x) = \int_{\Psi_I} T_z(x,y,z) d\Psi_I(y,z). \tag{4}$$

Similar expressions may be found for $\overline{f}_{s|f,x}(x)$ and $\overline{f}_{s|f,y}(y)$ by integrating T_x and T_y respectively. Here, the bar, $\overline{(\cdot)}$, indicates the quantity is per unit length.

For a beam whose cross-section is symmetric about the z-axis, the force per unit length applied in the y-direction is equal to zero. Furthermore, it is often the case that the applied force in the z-direction is much greater than that applied in the x-direction. As a result, when reviewing the beam theory in the following section, the applied force in the x-direction is momentarily neglected.

III. BEAM THEORY AND MODAL ANALYSIS

A. Equation of Motion for an Axially Loaded Beam in Vacuum

In this section, the equation of motion and modal properties for an axially loaded beam in vacuum is reviewed. Although the following derivation is for beams with axial loading, it is also valid for beams with no axial loading, and may be simplified by taking the axial force to be zero. In the remainder of the paper, a beam in vacuum without any fluid loading will be referred to as a bare beam. To begin, the equation of motion for a bare beam whose length is along the x-axis and direction of vibration is in the z-direction is [18]

$$EI\frac{\partial^4 w}{\partial x^4}(x,t) - P\frac{\partial^2 w}{\partial x^2}(x,t) + \rho_s A\frac{\partial^2 w}{\partial t^2}(x,t) = \overline{f}_z(x,t), \tag{5}$$

where x is the location on the beam, t is time, and w is the lateral displacement of the beam's neutral axis in the z-direction, E is the elastic modulus, I is the moment of inertia of the beam's cross-section, ρ_s is the mass density, A is the cross-sectional area, P is the axial force, and $\overline{f}_z(x,t)$ is the external force per unit length in the z-direction. The axial force is tensile when P is positive and compressive when P is negative. As the equation of motion in Eq. 5 is for motion in the z-direction, only forces in the z-direction are included. In Eq. 5, any intrinsic or material damping of the bare beam is ignored. This will be discussed in more detail in Sec. III C.

The lateral displacement of the beam may be expressed as a sum of the normal modes, such that

$$w(x,t) = \sum_{n=1}^{\infty} q_n(t)\phi_n(x), \tag{6}$$

where $\phi_n(x)$ is the n^{th} normal mode, and $q_n(t)$ is the mode's corresponding time dependent modal coordinate. Each normal mode satisfies the differential equation

$$EI\frac{d^4\phi_n(x)}{dx^4} - P\frac{d^2\phi_n(x)}{dx^2} - \omega_n^2\rho_s A\phi_n(x) = 0 \quad \text{for} \quad n = 1, 2, \ldots, \tag{7}$$

where ω_n is the undamped natural frequency for the n^{th} mode. The natural frequencies are related to the wavenumbers of the axially loaded beam by [19]

$$\beta_{\text{ax},n}^2 = -\frac{P}{2EI} \pm \sqrt{\left(\frac{P}{2EI}\right)^2 + \frac{\rho A\omega_n^2}{EI}}, \tag{8}$$

where $\beta_{\text{ax},n}$ are the roots to the frequency equation that satisfy the boundary conditions of the beam. For a beam with no axial load, such that $P = 0$, Eqs. 5 and 6 simplify to governing equations for a beam with no axial load. Likewise, the wavenumbers in Eq. 8 simplify to

$$\beta_n^4 = \frac{\rho A\omega_n^2}{EI}, \tag{9}$$

where β_n are the wavenumbers for a beam with no axial loading.

For the present work, the mode shapes in Eq. 6 are normalized such that the mode shape is equal to unity at a reference position on the beam. For a reference position, $\hat{x}_n$, it follows that

$$\phi_n(\hat{x}_n) = 1. \tag{10}$$

Furthermore, the undamped mode shapes follow the orthogonality condition [20]

$$\int_0^L \phi_m(x)\phi_n(x)dx = \begin{cases} 0 & m \neq n \\ \alpha_n & m = n \end{cases}, \tag{11}$$

where α_n is a modal constant of dimension length. It should be noted that the normalization convention in Eq. 10 is important for the present work, as it will allow for a convenient coordinate transformation to be made from physical to generalized coordinates. Such transformation will be essential when comparing the dynamic response of a resonator found from experimental measurements to that found from a 3D numerical model. For the present work, the reference position, $\hat{x}_n$, is the position at which the displacement response will be experimentally measured.

B. Equation of Motion for an Axially Loaded Beam Immersed in Fluid

For a beam immersed in a viscous fluid, a fluid force enters the equation of motion such that

$$EI\frac{\partial^4 w}{\partial x^4}(x,t) - P\frac{\partial^2 w}{\partial x^2}(x,t) + \rho_s A\frac{\partial^2 w}{\partial t^2}(x,t) = \overline{f}_z(x,t) + \overline{f}_{f|s,z}(x,t), \tag{12}$$

where $\overline{f}_{f|s,z}(x,t)$ is the force per unit length applied by the fluid to the beam in the z-direction. Due to equal and opposite forces at the interface, the force per unit length applied by the beam to the fluid is

$$\overline{f}_{f|s}(x,t) = -\overline{f}_{s|f}(x,t). \tag{13}$$

Substituting Eq. 13 into Eq. 12, the equation of motion for a fluid-loaded beam for motion in the z-direction is

$$EI\frac{\partial^4 w}{\partial x^4}(x,t) - P\frac{\partial^2 w}{\partial x^2}(x,t) + \rho_s A\frac{\partial^2 w}{\partial t^2}(x,t) + \overline{f}_{s|f,z}(x,t) = \overline{f}_z(x,t). \tag{14}$$

Here, we adopt the assumption that the fluid force may be expressed in terms of a damping force and inertial force. This formulation has been presented by Bao [21] and employed in previous works that analyzed miniaturized resonators vibrating in fluids [7, 8]. In the present work, we increase the accuracy of the fluid force expression by including a stiffness term that can model any compressibility of the fluid, such that

$$\overline{f}_{s|f,z}(x,t) = \overline{k}_f w(x,t) + \overline{c}_f\frac{\partial w}{\partial t}(x,t) + \overline{m}_f\frac{\partial^2 w}{\partial t^2}(x,t), \tag{15}$$

where $\overline{k}_f$, $\overline{c}_f$, and $\overline{m}_f$ are the effective stiffness, damping, and mass per unit length, respectively, of the fluid. Substituting Eq. 15 into Eq. 14, the equation of motion for the fluid-loaded beam is

$$EI\frac{\partial^4 w}{\partial x^4}(x,t) - P\frac{\partial^2 w}{\partial x^2}(x,t) + \rho_s A\frac{\partial^2 w}{\partial t^2}(x,t) + \overline{k}_f w(x,t) + \overline{c}_f\frac{\partial w}{\partial t}(x,t) + \overline{m}_f\frac{\partial^2 w}{\partial t^2}(x,t) = \overline{f}_z(x,t). \tag{16}$$

It should be noted that the expression for the fluid force in Eq. 15 is an approximation. The expression assumes that the fluid force at location x along the beam is proportional to the displacement and its time derivatives at the same x location. Furthermore, the expression assumes that the effective fluid stiffness, damping, and mass are independent of position and displacement amplitude. These assumptions result in a simplified expression for the fluid force which is amenable to modal analysis. Namely, as it will be shown in the following section, the fluid force in Eq. 15 gives rise to convenient expressions for effective modal fluid parameters.

C. Equation of Motion for a Bending Mode

The equation of motion for a bending mode of vibration is derived with use of the expansion theorem [22]. Here, the displacement response is expressed in terms of the modal sum in Eq. 6, which when substituted into Eq. 16 gives rise to

$$\begin{aligned} &EI\sum_{n=1}^{\infty}\frac{d^4\phi_n(x)}{dx^4}q_n(t) - P\sum_{n=1}^{\infty}\frac{d^2\phi_n(x)}{dx^2}q_n(t) + \rho_s A\sum_{n=1}^{\infty}\phi_n(x)\ddot{q}_n(t) + \cdots \\ &\overline{k}_f\sum_{n=1}^{\infty}\phi_n(x)q_n(t) + \overline{c}_f\sum_{n=1}^{\infty}\phi_n(x)\dot{q}_n(t) + \overline{m}_f\sum_{n=1}^{\infty}\phi_n(x)\ddot{q}_n(t) = \overline{f}_z(x,t). \end{aligned} \tag{17}$$

Equation 17 is simplified by applying the relationship in Eq. 7 which replaces the sum over the fourth and second order spatial derivative of $\phi_n(x)$, with a sum over $\phi_n(x)$. Further simplification is made by applying the orthogonality condition in Eq. 11 after multiplying the equation of motion throughout by an arbitrary mode, $\phi_m(x)$, and integrating from 0 to L. The resulting modal equation of motion of the fluid-loaded beam is

$$(K_{s,n} + K_{f,n})q_n(t) + C_{f,n}\dot{q}_n(t) + (M_{s,n} + M_{f,n})\ddot{q}_n(t) = \int_0^L \phi_n(x)\overline{f}_z(x,t)dx. \tag{18}$$

Capital variables indicate modal quantities, where $K_{s,n}$ and $M_{s,n}$ are the effective modal stiffness and mass of the solid bare beam given by

$$K_{s,n} = \alpha_n\omega_n^2\rho_s A \tag{19a}$$

$$M_{s,n} = \alpha_n \rho_s A, \tag{19b}$$

and $K_{f,n}$, $C_{f,n}$, and $M_{f,n}$ are the effective modal stiffness, damping, and mass due to fluid loading given by

$$K_{f,n} = \alpha_n \overline{k}_f \tag{20a}$$

$$C_{f,n} = \alpha_n \overline{c}_f \tag{20b}$$

$$M_{f,n} = \alpha_n \overline{m}_f. \tag{20c}$$

Here it should be noted that the equation of motion in Eq. 18 was derived for a bare beam with no material or intrinsic damping. For a bare beam with significant material damping, an effective modal damping parameter for the solid beam, $C_{s,n}$, may be added to Eq. 18. However, it is often the case that the modal damping of a bare beam, which is measured in vacuum, is of little consequence for the fluid dynamics problem: In dense liquids such as water, $C_{s,n}$ is orders of magnitude smaller than the fluidic dissipation. In gases, $C_{s,n}$ can be subtracted or is negligible compared to the fluid damping, especially for NEMS [5, 6, 23]. As a result, in the present work only the modal damping due to fluid loading, $C_{f,n}$, is considered in Eq. 18.

D. Forced Response

Finally, an expression for the forced response of a fluid-loaded beam may be derived by considering the frequency-dependent forcing function

$$\overline{f}_z(x,t) = f_0 \delta(x - \hat{x}_n) \exp(i\omega t), \tag{21}$$

where f_0 is the force amplitude with dimension force, $\delta(x - \hat{x}_n)$ is the Dirac delta function with dimension reciprocal length, and $\hat{x}_n$ is the reference position previously introduced in Eq. 10. Substituting Eq. 21 into Eq. 18 and evaluating the right-hand-side of the equation results in

$$\left((K_{s,n} + K_{f,n}) + i\omega C_{f,n} - \omega^2 (M_{s,n} + M_{f,n})\right) \widetilde{q}_n(\omega) = \widetilde{F}_n, \tag{22}$$

where $\widetilde{q}_n(\omega)$ is the frequency dependent complex-valued modal coordinate, and $\widetilde{F}_n$ is the modal force given by

$$\widetilde{F}_n = f_0 \phi_n(\hat{x}_n). \tag{23}$$

The tilde, $\tilde{(\cdot)}$, indicates quantities in the frequency domain. Note that the normalization condition in Eq. 10 relates the modal force directly to the force amplitude by $\widetilde{F}_n = f_0$. We now consider the transfer function between modal displacement and modal force, referred to as receptance [24], which is found to be

$$\widetilde{\chi}_n(\omega) \equiv \frac{\widetilde{q}_n(\omega)}{\widetilde{F}_n} \equiv \frac{1}{(K_{s,n} + K_{f,n}) + i\omega C_{f,n} - \omega^2 (M_{s,n} + M_{f,n})}. \tag{24}$$

The imaginary part of the receptance in Eq. 24 is found to be

$$\mathrm{Im}\left\{\widetilde{\chi}_n(\omega)\right\} = \frac{-\omega C_{f,n}}{\left[(K_{s,n} + K_{f,n}) - \omega^2 (M_{s,n} + M_{f,n})\right]^2 + \omega^2 C_{f,n}^2}. \tag{25}$$

From Eq. 25, the imaginary part of receptance is inversely proportional to $C_{f,n}$ near resonance. For this reason $\mathrm{Im}\left\{\widetilde{\chi}_n(\omega)\right\}$ will be later used to assess the damping due to fluid loading. With Eq. 25, $\mathrm{Im}\left\{\widetilde{\chi}_n(\omega)\right\}$ will be computed using modal properties of the bare beam and modal properties from the fluid loading predicted by the cylinder approximation. The validity of the cylinder approximation may then be examined by comparing $\mathrm{Im}\left\{\widetilde{\chi}_n(\omega)\right\}$ found from the cylinder approximation to that found experimentally and from numerical simulations.

IV. THE CYLINDER APPROXIMATION FOR HYDRODYNAMIC LOADING OF MECHANICAL RESONATORS

In this section, the 2D cylinder model for miniaturized resonators, such as microcantilevers and nanomechanical beams is reviewed. For slender bodies ($L \gg b, h$), such as microcantilevers and NEMS beams and strings, the structure is approximated as a long cylinder with diameter b oscillating perpendicular to its axis (in the z-direction) but in the mode shape of the structure. To derive the fluid force acting on the cylinder, a no-slip boundary condition at the surface of the cylinder is applied, and the following assumptions are made:

1. The cylinder is assumed to be of infinite extent perpendicular to its cross-section, i.e. in the x-direction and immersed in an infinite fluid medium;
2. the cross-section of the cylinder is uniform along its length;
3. the amplitude of oscillation is small, so that the Navier-Stokes equations can be linearized;
4. the fluid is assumed to be incompressible and a Newtonian fluid.

With the aforementioned assumptions, the complex-valued force per unit length applied by the fluid to a cylinder oscillating at frequency ω is [7]

$$\widetilde{\overline{f}}_{f|s,z}(x,\omega) = \frac{\pi}{4}\rho_f \omega^2 b^2 \Gamma_{\text{circ}}(\omega)\widetilde{w}(x,\omega), \tag{26}$$

where ρ_f is the fluid density, $\widetilde{w}(x,\omega)$ is the frequency dependent displacement amplitude of the cylinder in the z-direction and $\Gamma_{\text{circ}}(\omega)$ is the complex-valued dimensionless hydrodynamic function. The analytical expression for the hydrodynamic function is [25]

$$\Gamma_{\text{circ}}(\text{Re}) = 1 + \frac{4iK_1\left(-i\sqrt{i\text{Re}}\right)}{\sqrt{i\text{Re}}K_0\left(-i\sqrt{i\text{Re}}\right)} \tag{27}$$

where K_0 and K_1 are zeroth and first order modified Bessel functions of the second kind. The argument of Γ_{circ} is in terms of the frequency-dependent Reynolds number for the cylinder (and the beam) and is expressed as

$$\text{Re}(\omega, b) = \frac{\rho_f \omega b^2}{4\mu}. \tag{28}$$

where μ is the dynamic viscosity of the fluid. To account for the rectangular cross-section of a beam, one can apply a small Reynolds-number-dependent correction factor, $\Omega(\text{Re})$, of order one to $\Gamma_{\text{circ}}(\text{Re})$ and find the hydrodynamic function of a so-called oscillating blade [26]

$$\Gamma_{\text{rect}}(\text{Re}) = \Omega(\text{Re})\Gamma_{\text{circ}}(\text{Re}). \tag{29}$$

The blade approximation assumes the cylinder has vanishingly thickness. Consequently, in their current state, both the cylinder and blade approximation do not take into account the aspect ratio of the beam's rectangular cross-section [27].

From Eq. 26, the fluid force predicted from the cylinder approximation gives rise to an added effective mass and damping of the fluid, such that [28]

$$\overline{m}_{f,\Gamma} = \frac{\pi}{4}\rho_f b^2 \Gamma'(\omega), \tag{30a}$$

$$\overline{c}_{f,\Gamma} = \frac{\pi}{4}\rho_f \omega b^2 \Gamma''(\omega), \tag{30b}$$

where Γ' and Γ'' are the real and imaginary part, respectively, of the hydrodynamic function. Here the subscript on Γ is omitted to indicate that the hydrodynamic function may be computed from either the cylinder approximation in Eq. 27, or blade approximation in Eq. 29. Substituting Eq. 30 into Eq. 20, the effective modal mass and damping due to fluid loading predicted by the 2D cylinder approximation is

$$(M_{f,n})_\Gamma = \alpha_n \frac{\pi}{4}\rho_f b^2 \Gamma'(\omega) \tag{31a}$$

$$(C_{f,n})_\Gamma = \alpha_n \frac{\pi}{4} \rho_f \omega b^2 \Gamma''(\omega). \tag{31b}$$

With the effective modal properties in Eq. 31 and the modal equation of motion in Eq. 18, an expression for the undamped natural frequencies of a fluid-loaded beam is found to be

$$(\hat{\omega}_n)_\Gamma^2 = \omega_n^2 \frac{1}{1 + T_0 \Gamma'(\omega_n)}, \tag{32}$$

where $(\hat{\omega}_n)_\Gamma$ and ω_n are the undamped natural frequencies of the fluid-loaded and bare beam, respectively, and T_0 is a mass loading parameter equal to the ratio of the mass of cylinder of fluid to the mass of the beam [8], such that

$$T_0 = \frac{\pi}{4} \frac{\rho_f b}{\rho_s h}. \tag{33}$$

An expression for the modal damping ratio is also found to be

$$2\,(\zeta_n)_\Gamma = \frac{\omega_n}{(\hat{\omega}_n)_\Gamma} \frac{\Gamma''(\omega_n)}{1/T_0 + \Gamma'(\omega_n)}. \tag{34}$$

For gas experiments T_0 is very small [6] such that $1/T_0 \gtrsim 1000 \gg \Gamma'$ and the mass loading can be neglected. Thus the undamped natural frequency of the fluid-loaded beam may be approximated as $(\hat{\omega}_n)_\Gamma \approx \omega_n$, and the modal damping ratio may be approximated as $2\,(\zeta_n)_\Gamma \approx T_0 \Gamma''(\omega)$. As a result, the imaginary component of the hydrodynamic function is found directly from the modal damping ratio or quality factor which is related by $Q_n = 1/(2\zeta_n)$, such that

$$\frac{1}{(Q_n)_\Gamma} \approx T_0 \Gamma''(\omega). \tag{35}$$

V. METHODS

A. Experimental Methods

Our experiments are performed on nanomechanical silicon nitride doubly-clamped beam resonators under tension. Figure 1a shows a scanning electron microscope (SEM) image of a typical beam that has linear dimensions of $L \times b \times h \approx 40\ \mu\text{m} \times 950\ \text{nm} \times 93\ \text{nm}$. There is a $g \approx 2\ \mu$m gap between the beam and the substrate. There are two metal (gold) u-shaped electrodes on each end of the beam, through which AC electric current can be passed. This causes Ohmic heating cycles, which in turn generate thermal bending moments due to the mismatch in the thermal expansion coefficients of the structural layers. The result is efficient actuation of nanomechanical oscillations at exactly twice the frequency of the applied AC current [29, 30]. Both the driven and random motions of the beams are measured using a path-stabilized Michelson interferometer [31]. For the fundamental mode, transverse displacement in the z-direction, $w(x,t)$, is measured at the center of the beam where $x = L/2$; for higher modes, $w(x,t)$ is measured at anti-node positions.

In Sec. VI A, measurements on two silicon nitride doubly-clamped beams are presented. The beams are under tension with identical cross-sectional dimensions of $b \times h \approx 950\ \text{nm} \times 93\ \text{nm}$; the lengths are $L \approx 60$ and $50\ \mu$m; the gap distance is the same in both $g \approx 2\ \mu$m. The experiments were performed in air at atmospheric pressure and in water, both at room temperature $T = 293$ K. For the experiments in water, the fluid dynamics is in the continuum viscous limit and the Navier-Stokes equations are solved for the analysis with a no-slip boundary condition on the beam and substrate. The experimental conditions in air correspond to a Knudsen number of $\text{Kn}_l \approx 0.06$ and generalized Knudsen number of $\text{Kn}_l + \text{Wi} \approx 0.07$ [6], suggesting that the rarefaction effects may be at play [32, 33]. From our previous work [5, 6, 23, 34], however, we estimate that the rarefaction (and slip) is not so significant and continuum theory approximates the fluid dynamics of these devices quite well. Consequently, the NEMS data in air here are also fit and analyzed by continuum theory. The density of air is taken to be $\rho_f = 1.2042\ \text{kg/m}^3$ for the following analyses and numerical models.

It must be emphasized that there is some uncertainty in the material properties of our silicon nitride beams [35]. The density ρ_s and Young's modulus E of silicon nitride depend on deposition conditions and vary from sample to sample. Since we did not have direct measurements, the material properties and axial tension used in the following analyses and numerical models were found by minimizing the error between predicted and measured natural frequencies of the beam in air [36]. The search algorithm found the optimal value of elastic modulus, E, and axial load, P, for a fixed

value of beam density, ρ_s. For the present work, the density was taken to be $\rho_s = 3{,}350$ kg/m^3, which falls within the range, 2,600 kg/m^3 $\leq \rho_s \leq$ 3,400 kg/m^3, of reported values for silicon nitride [37–39]. Our E, P and ρ_s values depend on the optimization process, the linear dimensions and the various assumptions made, and small but inconsequential discrepancies [35] are unavoidable.

B. Numerical Methods

1. *Construction and Evaluation of 3-Dimensional Finite Element Model*

In this section, the 3D FEM used to analyze MEMS/NEMS resonators immersed in a viscous fluid is discussed. For the present work, all FEMs were constructed and analyzed using commercial software COMSOL Multiphysics®[40]. The model consists of a beam surrounded by a sphere of fluid. The 3D model is depicted in Fig. 2a, where only half of the beam and spherical fluid domain are shown and analyzed due to the symmetry about the x-z plane. A corresponding 2D drawing with dimensions used in the model is depicted in Fig. 2b. The fluid is modeled with two concentric spheres surrounding the 3D solid beam. The fluid domain within the sphere of radius R_1 is modeled with a Thermoviscous Acoustics solver to capture all the thermal and viscous losses that occur in the boundary layers. In this domain, the fluid is modeled as a viscous compressible Newtonian fluid with the following frequency domain equations: momentum equation, continuity equation, energy conservation equation, and linearized equation of state. By modeling the fluid near the beam as a viscous compressible Newtonian fluid, the total effect of the fluid-structure interaction may be observed. Namely, the fluid is capable of applying a stiffness, damping, and inertial force to the beam. Analysis of the fluid force will be pertinent when analyzing the vibration of NEMS beams near a substrate and the effects of squeeze film damping. Specifically, the real part of the fluid force, which is dependent on the compressibility and added mass of fluid, will be analyzed to observe changes in the hydrodynamic function. In the outer spherical layer between R_1 and R_2, the fluid is modeled as a compressible lossless fluid and is governed by the Helmholtz equation. More details on the governing equations may be found in Appendix A.

The radius R_1 is chosen such that the fluid is approximately quiescent at R_1, allowing for all viscous and thermal losses to be captured within the inner spherical layer. In this domain, a fine mesh is needed near the beam to accurately capture all the losses in the boundary layer. A convergence study on the mesh size is presented in Appendix B. In the outer spherical layer between R_1 and R_2, the fluid is modeled to be lossless, such that the power radiated through a spherical surface is constant for any radial distance between R_1 and R_2. This allows a spherical wave radiation boundary condition to be applied at the outer spherical surface. It is important to note that for all measured and simulated devices, the effect of acoustic radiation is minimal. Specifically, the parameters of the devices have been chosen such that the energy loss due to acoustic radiation is negligible due to the small amount of acoustic waves generated in the fluid. Since the fluid is approximately quiescent at R_1, the lossless outer spherical layer mainly serves the purpose of creating a domain that is amenable to the spherical wave boundary condition. Boundary conditions will be further discussed in the following paragraph. Convergence studies that analyze how the FEM results depend on radii R_1 and R_2 are presented in Appendix B.

For cases where there is no substrate, the fluid is modeled as an infinite medium by imposing a spherical wave radiation boundary condition at the outer spherical boundary. This boundary condition allows an outgoing spherical wave to leave the domain with minimal reflection. When a substrate is present, a wall is modeled at a gap distance, g, below the beam as depicted in Fig. 2c. At the wall, boundary conditions are imposed such that the normal component of fluid acceleration and velocity are zero. At the fluid-structure interface, the fluid is coupled to the solid beam such that the boundary conditions in Eqs. 1 and 2 are satisfied.

With the constructed FEM, the response of a resonator immersed in fluid may be analyzed with either a forced response simulation or an eigenfrequency simulation. In the forced response simulation, the beam is excited with a distributed load that has the spatial form of Eq. 21, and a force amplitude, f_0, that remains constant across frequency. The frequencies of excitation are chosen close to the resonance frequency of interest such that the response of the beam is dominated by the excited mode. At each excitation frequency, the forced response of the beam, as well as the fluid field, is found. In contrast, when an eigenfrequency simulation is performed, the complex-valued mode shape of the beam and fluid are found for the corresponding complex-valued eigenfrequency. This predicts the shape of the deformed beam and fluid field that oscillate at the corresponding complex-valued natural frequency. Evaluation of the complex eigenvalue problem allows for the undamped natural frequency and quality factor of the fluid-loaded beam to be predicted exactly, while avoiding approximations made in Sec. III. Such simulation will be important when predicting the quality factor of higher modes, where loading may also occur in the x-direction, resulting in additional energy dissipation.

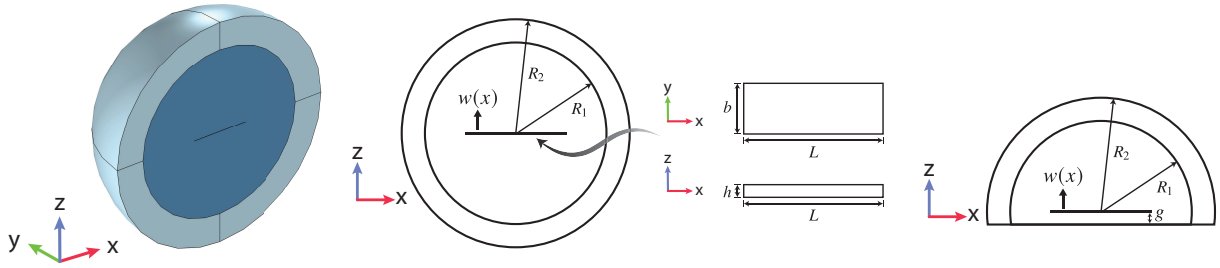

(a) (b) (c)

FIG. 2. (a) 3D FEM of a beam immersed in an infinite fluid medium. (b) 2D drawing with dimensions for model of a beam in an infinite fluid medium. (c) 2D drawing with dimensions for model of a beam in fluid with a substrate.

2. *Post-Processing of 3-Dimensional Finite Element Model*

In this section, methods for evaluating quantities that will be discussed in Sec. VI are presented.

Receptance With the solution to the forced response simulation, the receptance in Eq. 24 is evaluated by solving for the frequency dependent modal amplitude, $\widetilde{q}_n(\omega)$. The modal amplitude is found by approximating light modal coupling near resonance, such that the modal amplitude is related to the beam displacement and mode shape by

$$\widetilde{w}(x,\omega) \approx \widetilde{q}_n(\omega)\phi_n(x). \tag{36}$$

With the solution to the 3D FEM and beam displacement $\widetilde{w}(x,\omega)$, the modal amplitude may be found from a simple change of coordinate by evaluating the displacement at the reference position, $\hat{x}_n$, such that

$$\widetilde{q}_n(\omega) \approx \frac{\tilde{w}(x=\hat{x}_n,\omega)}{\phi_n(\hat{x}_n)}. \tag{37}$$

The receptance may then be evaluated with use of Eq. 24. To enable the comparison between numerical results and experimental measurements, the reference position for the fundamental mode in Eqs. 10 and 37 is taken to be $\hat{x}_1 = L/2$, which is the same location at which the displacement is experimentally measured.

Hydrodynamic Function The hydrodynamic function introduced in Sec. IV may be found from the solution to either a forced response simulation or eigenfrequency simulation. For ease of discussion, the expression for the force per unit length applied by the beam to the fluid in Eq. 26 is repeated here

$$\left(-\frac{\pi}{4}\rho_f\omega^2 b^2\Gamma(\omega)\right)\widetilde{w}(x,\omega) = \widetilde{\overline{f}}_{s|f,z}(x,\omega). \tag{38}$$

Equation 38 can be simplified to

$$\widetilde{\overline{\kappa}}(\omega)\widetilde{w}(x,\omega) = \widetilde{\overline{f}}_{s|f,z}(x,\omega), \tag{39}$$

where $\widetilde{\overline{\kappa}}$ is the dynamic stiffness per unit length, which was set equal to the the quantity in parentheses in Eq. 38. Rearranging Eq. 39, the dynamic stiffness is expressed as

$$\widetilde{\overline{\kappa}}(\omega) = \frac{\widetilde{\overline{f}}_{s|f,z}(x,\omega)}{\widetilde{w}(x,\omega)}. \tag{40}$$

The right-hand-side of Eq. 40 is dependent on position, as it is the ratio of force to displacement along the length of the beam. However, based on the formulation of the approximation presented in Sec. IV, the hydrodynamic function, and therefore $\widetilde{\overline{\kappa}}$, is assumed to be constant and independent of position. Therefore, for the present work the dynamic stiffness is found by taking an effective spatial average, such that

$$\widetilde{\overline{\kappa}}(\omega) = \frac{\int_0^L \widetilde{w}^*(x,\omega)\widetilde{\overline{f}}_{s|f,z}(x,\omega)dx}{\int_0^L \widetilde{w}^*(x,\omega)\widetilde{w}(x,\omega)dx}, \tag{41}$$

where $\widetilde{w}^*(x,\omega)$ is the complex conjugate of the beam displacement. Substituting the expression for force applied by the beam to the fluid in Eq. 4, into Eq. 41, and simplifying the denominator, the dynamic stiffness is found to be

$$\widetilde{\overline{\kappa}}(\omega) = \frac{\int_0^L \int_{\Psi_I} \widetilde{w}^*(x,\omega)\widetilde{T}_z(x,y,z,\omega)d\Psi_I dx}{\int_0^L ||\widetilde{w}(x,\omega)||^2 dx}. \tag{42}$$

As a result, with the solution to the 3D FEM, the computed displacement response of the beam and the traction at the fluid structure interface may be used to compute the dynamic stiffness in Eq. 42. With the computed dynamic stiffness, $\widetilde{\overline{\kappa}}$, the hydrodynamic function may then be computed with

$$\Gamma_{\text{sim}}(\omega) = \frac{\widetilde{\overline{\kappa}}}{-\frac{\pi}{4}\rho_f \omega^2 b^2}. \tag{43}$$

Quality Factor As mentioned in the prevision section, Sec. V B 1, an eigenfrequency simulation may be performed to find the exact modal properties of the fluid-loaded beam. The eigenfrequency simulation solves the complex eigenvalue problem for the complex eigenvalue, Λ_n, which is related to the undamped natural frequency and modal damping ratio by

$$\Lambda_n = \omega_n \left(i\zeta_n \pm \sqrt{1-\zeta_n^2} \right). \tag{44}$$

With the computed complex eigenvalue, the undamped natural frequency may then be computed by taking the absolute value of Eq. 44, and the quality factor may be computed from

$$Q_n = \frac{1}{2}\left(\frac{\text{abs}\{\Lambda_n\}}{\text{Im}\{\Lambda_n\}} \right). \tag{45}$$

VI. RESULTS

A. Effect of a Substrate: Squeeze Damping

When a wall is placed in proximity to a vibrating resonator, the entire velocity field (not just the field in the gap) is modified. This is observed in Fig. 3, which plots the local fluid velocity field, $\sqrt{\Sigma_{i=1}^3 ||v_{f,i}||^2}$, normalized to the magnitude of the beam velocity for a resonator vibrating near a substrate and in an infinite medium. The 2D fluid field ($y-z$ plane) shown in Fig. 3 is in the middle ($x = L/2$) of a doubly-clamped beam vibrating in its fundamental mode. The velocity of the beam's cross-section is depicted with the yellow velocity arrow, and the fluid velocity field is depicted with black velocity arrows, whose direction is proportional to the velocity in the y and z-direction. Figure 3a shows that as the beam moves towards the substrate, the fluid is squeezed, with some fluid flowing out of the gap. The presence of a substrate thus results in a change in the fluid pressure and stress field, which consequently modifies the fluid loading of the beam [10].

The effect of a substrate is illustrated in Fig. 4 which plots the magnitude of the imaginary part of receptance, $||\text{Im}\{\tilde{\chi}_1(\omega)\}||$, for the 50 μm doubly-clamped NEMS beam discussed in Sec. V A. Here, the NEMS beam is vibrating in its fundamental mode in air. The figure compares the experimentally measured receptance to the receptance evaluated with the blade approximation and numerical simulation. Here, the blade approximation is used in place of the cylinder approximation due to the relatively small thickness to width aspect ratio of the beam. Experimentally, the receptance was found from the measured power spectral density (PSD), which is related to receptance by [8]

$$G_f(\omega) = -\frac{4k_B T}{\omega}\text{Im}\{\tilde{\chi}(\omega)\}, \tag{46}$$

where k_B is the Boltzmann constant, and T is temperature. In Fig. 4a, a base-10 logarithmic scale and linear scale are used to plot receptance in the main part and inset of the figure.

In Fig. 4a, the solid blue line is the magnitude of the imaginary part of receptance evaluated with Eq. 25 using modal fluid properties predicted with the blade approximation in Eq. 31, and modal properties of the bare beam evaluated with Eq. 19 using the optimized material properties. From Fig. 4a, the blade approximation under-predicts the damping due to fluid loading when a substrate is present. This is observed by comparing the amplitude of $||\text{Im}\{\tilde{\chi}_1(\omega)\}||$ near resonance. From Eq. 25, a decrease in $||\text{Im}\{\tilde{\chi}_1(\omega)\}||$ near resonance corresponds to an increase in damping. This increase in damping is due to the increase in fluid stress, and thus fluid loading applied to the beam.

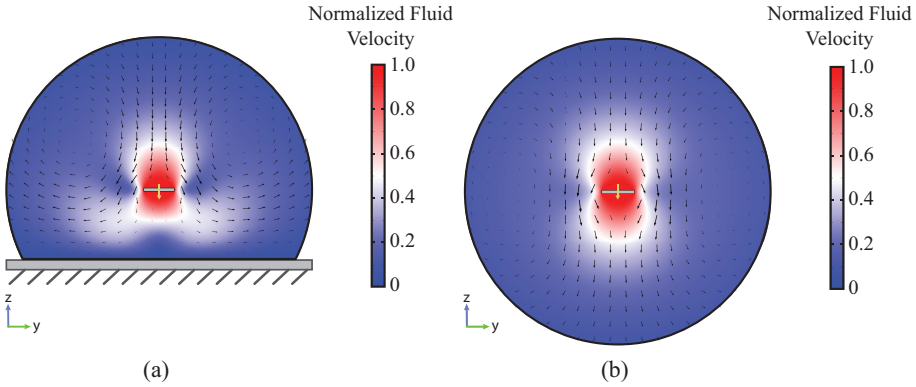

FIG. 3. Color plots of normalized fluid velocity, $\sqrt{\Sigma_{i=1}^{3}||v_{f,i}||^2}/||\dot{w}||$, with velocity arrow field in the $y-z$ plane for a doubly-clamped beam vibrating in its fundamental mode in air. (a) Resonator is near a substrate with a $g = 2$ μm gap distance and dimensionless squeeze number $\Pi_{\text{sq}} = 0.816$. (b) Resonator is in an infinite fluid.

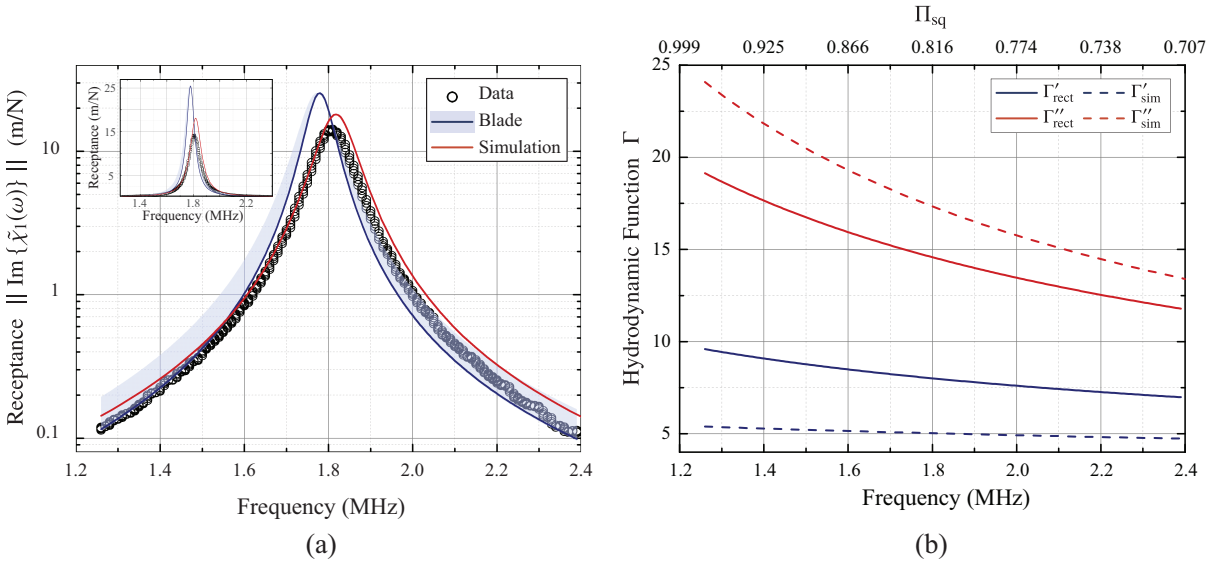

FIG. 4. Results for 50 μm NEMS beam in air. (a) Magnitude of the imaginary part of receptance $||\text{Im}\{\chi(\omega)\}||$, versus frequency for data, blade approximation, and simulation. $||\text{Im}\{\chi(\omega)\}||$ plotted with base-10 logarithmic scale (main) and linear scale (inset). The shading indicates the uncertainty cloud of the cylinder model which was obtained by evaluating the receptance for the beam density range 2,600 kg/m^3 $\leq \rho_s \leq$ 3,400 kg/m^3. (b) Real, $\Gamma'(\omega)$, and imaginary, $\Gamma''(\omega)$, part of hydrodynamic function versus frequency (lower axis) and dimensionless squeeze number (upper axis), Π_{sq}, for blade approximation and simulation.

From Fig. 4a, the numerical simulation better captures the increase in damping due to the presence of a substrate. This is depicted by the decrease in amplitude of $||\text{Im}\{\tilde{\chi}_1(\omega)\}||$ near resonance, resulting in better agreement with the experimentally obtained receptance. Additionally, the receptance found with the blade approximation is evaluated for the beam density range 2,600 kg/m^3 $\leq \rho_s \leq$ 3,400 kg/m^3, and is plotted with the shaded blue region in Fig. 4a. For a given density value, ρ_s, the modal stiffness and mass of the bare beam are computed with Eq. 19. Note that from Eq. 19 and the analysis presented in Sec. III, the modal parameters of the bare beam only depend on the solid density and natural frequency. Also note that the modal mass and damping due to fluid loading predicted by the blade approximation in Eq. 31 are independent of the beam density. As a result, by evaluating the receptance with Eq. 25 from modal properties computed for a range of reported silicon nitride density values, the range in receptance represents all possibles responses of the silicon nitride resonator predicted with the blade approximation. The results indicate that the observed trends in damping predicted by the blade approximation is independent of the material properties used to model the bare beam. Specifically, it is observed that the blade approximation under-predicts the damping due to fluid loading for all practical values of beam material properties when a substrate is present.

Figure 4b plots the hydrodynamic function, Γ, found from the blade approximation and numerical simulation. Both the real, Γ', and imaginary, Γ'', part of the hydrodynamic function are plotted. First considering the imaginary part of the hydrodynamic function, it is shown that the blade approximation, Γ''_{rect}, is less than the numerical simulation, Γ''_{sim}, and thus under-predicts the damping. This is to be expected from the results observed in Fig. 4a. In contrast, the real part of the hydrodynamic function found from the blade approximation, Γ'_{rect}, is greater than that found from the numerical simulation, Γ'_{sim}. This does not necessarily imply that the blade approximation over-predicts the added mass of the fluid. Instead, one can only conclude that the blade approximation over-predicts the real part of the fluid force applied to the beam. Recalling Sec. V B 2, the hydrodynamic function found from the numerical simulation is proportional to the dynamic stiffness, $\widetilde{\overline{\kappa}}$, by virtue of Eq. 43. The dynamic stiffness found from the numerical simulation and Eq. 42 is complex-valued, and may be interpreted with use of Eqs. 15 and 40. It follows that the real part of the dynamic stiffness, $\widetilde{\overline{\kappa}}'$, can be interpreted as

$$\widetilde{\overline{\kappa}}'(\omega) = \overline{k}_f - \omega^2 \overline{m}_f, \tag{47}$$

where $\overline{k}_f$ and $\overline{m}_f$ are the effective stiffness and mass of the fluid, respectively. In the numerical simulation, the fluid is modeled as compressible, and the compressibility could in principle result in added stiffness. This type of added stiffness has been discussed in the MEMS literature [10]. From Eq. 47, however, the total contribution of any stiffness increase or mass loading presented by the fluid are entangled. Consequently, the exact contribution of the stiffness change or mass loading cannot be readily determined, as the numerical simulation only finds the real part of the dynamic stiffness. From Fig. 4b, the blade approximation's inaccuracy in predicting the real part of the hydrodynamic function is attributed to its inaccuracy in predicting any stiffness or mass loading when a substrate is present. It should be noted that the Mach number, the ratio of velocity amplitude to sound speed in air, is $\text{Ma} \approx 0$. This is due to the NEMS beam's very small amplitude of vibration of $\mathcal{O}(1)$ nm. While this simple assessment suggests that the fluid is practically incompressible, past work have discussed stiffness changes in MEMS due to fluid compression [10], suggesting that more involved analyses may be needed. Such detailed analysis of frequency trends, which is out of the scope of this current paper.

Additional results depicting the effect of a substrate are presented in Fig. 5, which plots results for the 50μm doubly-clamped NEMS beam vibrating in its first mode in water [35]. From Fig. 5a, disagreement between the blade approximation and data are observed below and near resonance, as the approximation is unable to capture the effect of the substrate. In contrast, better agreement is obtained with the numerical simulation, which better predicts the fluid force applied to the beam. Interestingly, the blade approximation begins to match the numerical simulation at higher frequencies above resonance, as depicted in both Figs. 5a and 5b. At higher frequency ranges, it is observed that the hydrodynamic function found from the blade approximation begins to approach that found from the numerical simulation. This implies that at such frequencies, the presence of a substrate does not effect the fluid field and the force applied to the beam by the fluid. Similar trends are observed in Fig. 6, which plots results for the 60 μm doubly-clamped NEMS beam vibrating in its first mode in water [35]. The longer length results in a lower resonance frequency and therefore a larger viscous boundary layer and dimensionless squeeze number. Below and near resonance the simulation agrees well with data, whereas the blade approximation inaccurately predicts the beam's response. The larger dimensionless squeeze number results in larger disagreement between the hydrodynamic function predicted with the blade approximation and simulation, as depicted in Fig. 6b. At higher frequencies above resonance, the effect of the substrate becomes less prominent. However, both the simulation and blade approximation show disagreement with data due to strong modal coupling and the consequent break down of the single degree-of-freedom modal analysis formulation.

To quantify the effect of a substrate, the following dimensionless squeeze number is introduced

$$\Pi_{\text{sq}} = \frac{\delta_{\text{visc}}}{g}, \tag{48}$$

where g is the gap distance between the resonator and substrate, and δ_{visc} is the viscous boundary layer thickness

$$\delta_{\text{visc}}(\omega) = \sqrt{\frac{2\mu}{\rho_f \omega}}. \tag{49}$$

When Π_{sq} is near unity, such that $\delta_{\text{sq}} \approx g$, the presence of the substrate will greatly effect the fluid field and force applied to the beam. This was previously observed in Fig. 3a, which plotted the velocity field for a resonator near a substrate with a gap distance of $g = 2$ μm and dimensionless squeeze number $\Pi_{\text{sq}} = 0.816$. The effect of a substrate may also be observed by considering the viscous dissipation function, defined as the power dissipated per unit volume due to viscous losses, and expressed as the following double dot product [41]

$$\Delta_{\text{visc}} = \boldsymbol{\tau}_f : \nabla \mathbf{v}_f, \tag{50}$$

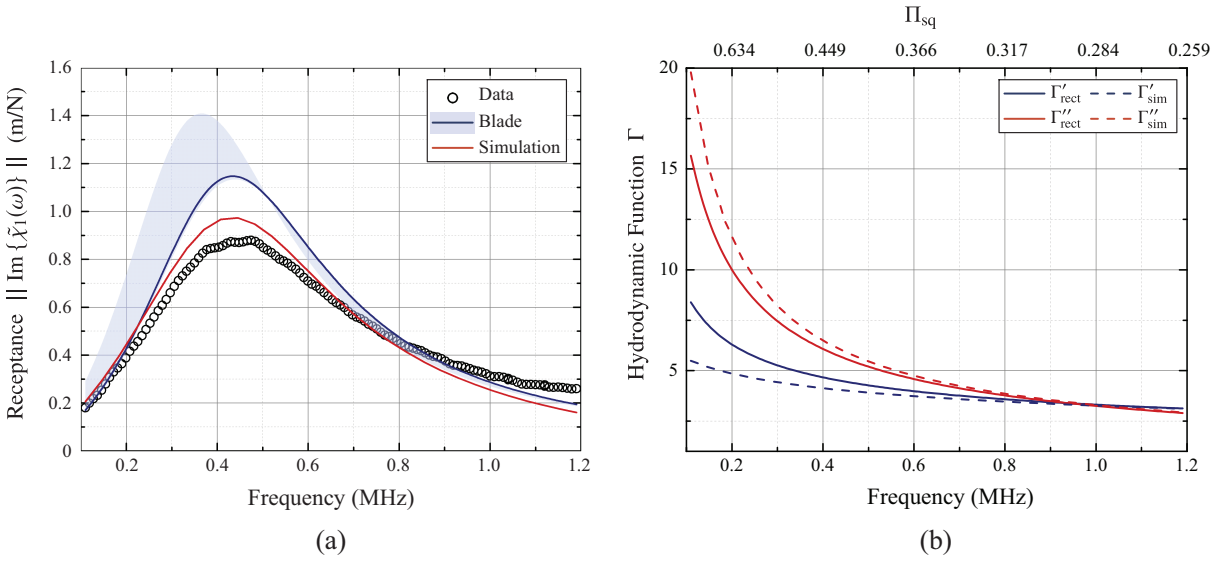

FIG. 5. Results for 50 μm NEMS beam in water. (a) Magnitude of the imaginary part of receptance $||\mathrm{Im}\{\chi(\omega)\}||$, versus frequency for data, blade approximation, and simulation. The shading indicates the uncertainty cloud of the cylinder model which was obtained by evaluating the receptance for the beam density range 2,600 kg/m^3 $\leq \rho_s \leq$ 3,400 kg/m^3. (b) Real, $\Gamma'(\omega)$, and imaginary, $\Gamma''(\omega)$, part of hydrodynamic function versus frequency (lower axis) and dimensionless squeeze number (upper axis), Π_{sq}, for blade approximation and simulation.

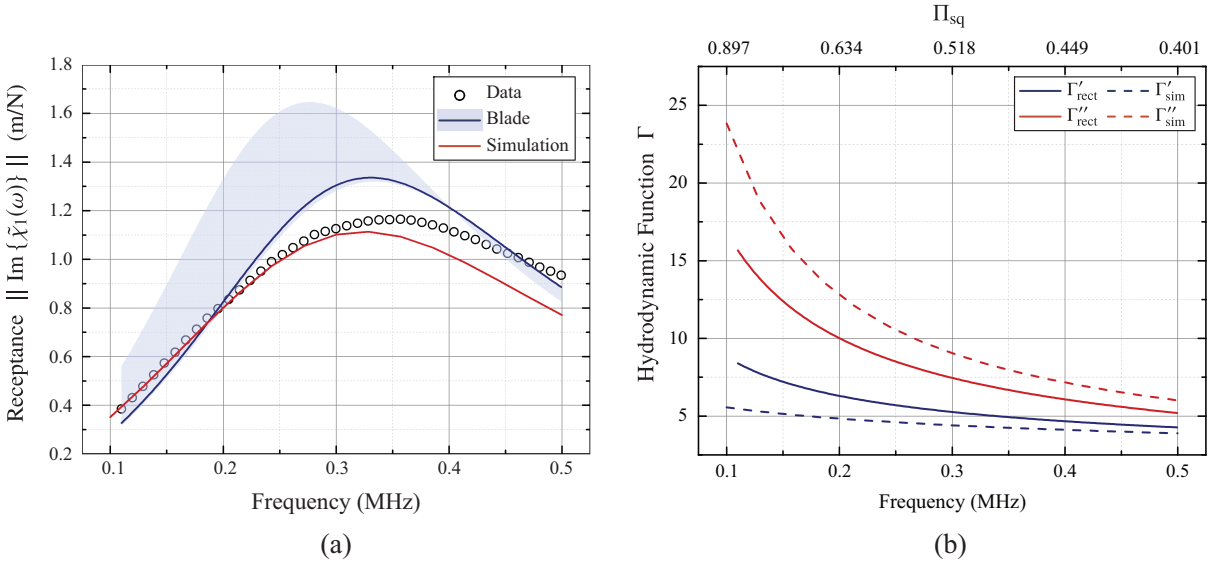

FIG. 6. Results for 60 μm NEMS beam in water. (a) Magnitude of the imaginary part of receptance $||\mathrm{Im}\{\chi(\omega)\}||$, versus frequency for data, blade approximation, and simulation. The shading indicates the uncertainty cloud of the cylinder model which was obtained by evaluating the receptance for the beam density range 2,600 kg/m^3 $\leq \rho_s \leq$ 3,400 kg/m^3. (b) Real, $\Gamma'(\omega)$, and imaginary, $\Gamma''(\omega)$, part of hydrodynamic function versus frequency (lower axis) and dimensionless squeeze number (upper axis), Π_{sq}, for blade approximation and simulation.

where $\boldsymbol{\tau}_f$ is the viscous fluid stress tensor and $\nabla \mathbf{v}_f$ is the fluid velocity gradient tensor.

Figure 7 plots the logarithm of the viscous dissipation function normalized to the maximum viscous dissipation function in the fluid field for the same resonators analyzed in Fig. 3. In both Fig. 7a and 7b, relatively large dissipation occurs near the resonator due to the viscous boundary layer that forms at the oscillating solid interface. Furthermore, from Fig. 7a, an additional boundary layer forms at the substrate due to the fluid flowing out of the gap and the no-slip boundary condtion at the wall, resulting in viscous stresses that dissipate energy. To observe the dependence on gap distance and Π_{sq}, the logarithm of the normalized viscous dissipation function is plotted in Fig. 8a, for a

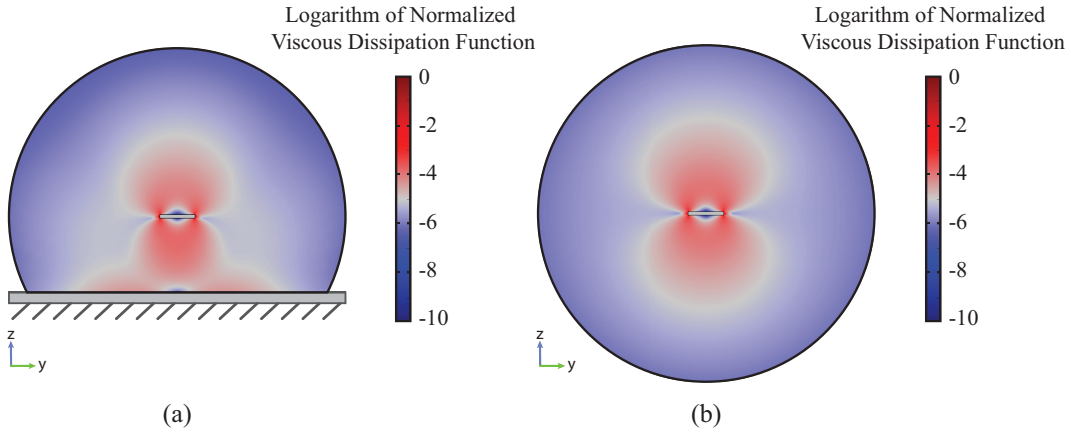

FIG. 7. Logarithm of normalized viscous dissipation function, $\log_{10}(\Delta_{\text{visc}}/\max\{\Delta_{\text{visc}}\})$, in the $y-z$ plane for a doubly-clamped beam vibrating in its fundamental mode in air. (a) Resonator is near a substrate with a $g = 2$ μm gap distance and dimensionless squeeze number $\Pi_{\text{sq}} = 0.816$. (b) Resonator in an infinite fluid.

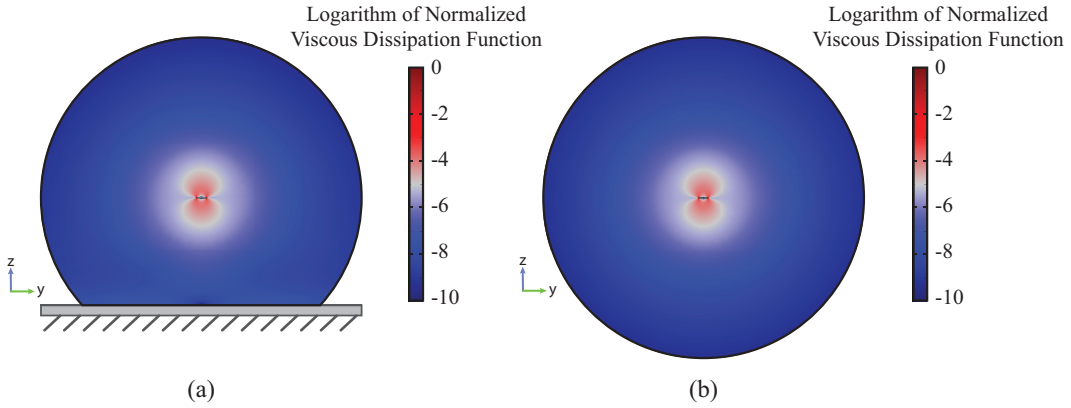

FIG. 8. Logarithm of normalized viscous dissipation function, $\log_{10}(\Delta_{\text{visc}}/\max\{\Delta_{\text{visc}}\})$, in the $y-z$ plane for a doubly-clamped beam vibrating in its fundamental mode in air. (a) Resonator is near a substrate with a $g = 10$ μm gap distance and dimensionless squeeze number $\Pi_{\text{sq}} = 0.163$. (b) Resonator is in an infinite fluid.

resonator near a substrate with a gap distance of $g = 10$ μm and dimensionless squeeze number $\Pi_{\text{sq}} = 0.163$. The fluid field may be compared to Fig. 8b, which plots the fluid field for a resonator vibrating in an infinite fluid medium. Comparing Figs. 8a and 8b, it is observed that the presence of the substrate has no visible effect on the fluid field and the viscous losses. This is because the gap distance, g, is much greater than the viscous boundary layer thickness, δ_{visc}, and the substrate is in a region of the fluid which is seemingly quiescent. As a result, the effect of the substrate tends to decrease with the decrease in dimensionless squeeze number.

To better illustrate the dependence on the dimensionless squeeze number, Π_{sq}, a numerical parametric study was performed. In the parametric study, the gap distance, g, between the resonator and substrate was increased from $g = 1$ μm to $g = 10$ μm. At each gap distance, the fluid force applied to the beam was evaluated, and the corresponding real and imaginary part of the hydrodynamic function, Γ'_{sub} and Γ''_{sub}, respectively, were computed. An identical resonator vibrating in an infinite fluid was then simulated, and the real and imaginary part of the hydrodynamic function, Γ'_{inf} and Γ''_{inf}, were evaluated. The results to the parametric study are shown in Fig. 9, which plots the real and imaginary components of the hydrodynamic function found for the resonator near a substrate, normalized to that found for the resonator in an infinite fluid. The results are plotted versus gap distance, g, and dimensionless squeeze number, Π_{sq}. Here, it is shown that for small g and large Π_{sq}, the presence of the substrate greatly effects the fluid load and the resulting hydrodynamic function. In agreement with previous results, the imaginary part of the hydrodynamic function, which quantifies the fluidic dissipation and effective damping applied to the beam, increases when a substrate is present, indicative of $\Gamma''_{\text{sub}}/\Gamma''_{\text{inf}} > 1$. However, as the gap distance increases and the dimensionless squeeze number, Π_{sq}, decreases, the effect of the substrate decreases and Γ''_{sub} approaches Γ''_{inf}. A similar trend is observed for the real part of the hydrodynamic load. However, for this case, when the gap distance is small, the

presence of a substrate modifies the effective modal stiffness and mass of the fluid, resulting in $\Gamma'_{\text{sub}} < \Gamma'_{\text{inf}}$. The trends observed in Fig. 9 are reflected in previous results. Recalling Fig. 5b, with increasing frequency, the viscous boundary layer in Eq. 49 decreases, and thus the dimensionless squeeze number in Eq. 48 also decreases. As a result, the presence of the substrate is seen to have less effect on the fluid field and resulting hydrodynamic function at higher frequencies, where Γ_{sim} begins to approach Γ_{rect}.

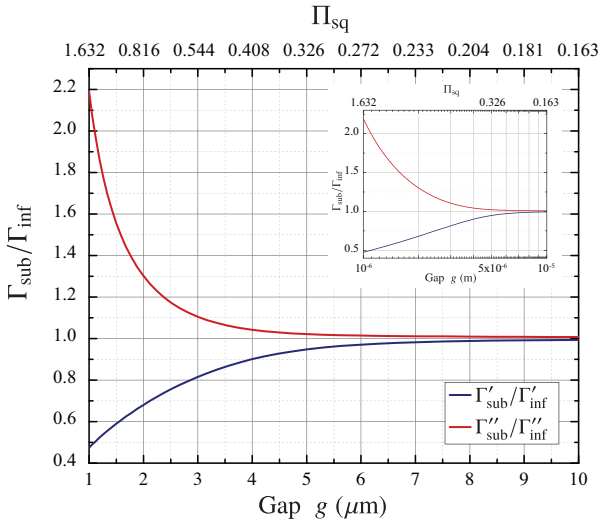

FIG. 9. Hydrodynamic function for a resonator near a substrate, Γ_{sub}, normalized to hydrodynamic function for resonator in an infinite medium, Γ_{inf}, versus gap distance (lower axis), g, and dimensionless squeeze number (upper axis), Π_{sq}. Gap distance and dimensionless squeeze number plotted with linear scale (main) and base-10 logarithmic scale (inset).

To conclude this section, the range on Π_{sq} for which the substrate may be approximately neglected is discussed. As observed in Fig. 9, the effect of the substrate becomes negligible for very small values of the dimensionless squeeze number, $\Pi_{\text{sq}} \ll 1$. This limit occurs when the substrate is far from the beam, or the frequency of oscillation is relatively large such that the boundary layer thickness is relatively small. Considering the imaginary part of the hydrodynamic function which predicts dissipation, results from the parametric study found that $\Gamma''_{\text{sub}}/\Gamma''_{\text{inf}} \approx 1.05$ at $\Pi_{\text{sq}} = 0.4307$. Hence, the error due to neglecting the substrate was limited to 5% when $\Pi_{\text{sq}} < 0.4307$. As these computed errors are specific to the numerical study, additional detailed sensitivity studies must be conducted to determine accurate bounds on Π_{sq}. However, all results in the present work support the conclusion that the substrate can not be neglected when $\Pi_{\text{sq}} \approx 1$.

B. Axial Flow

In this section, the effect of flow along the axis of a beam (x-direction) is examined. As discussed in Sec. IV, the cylinder and blade approximation are derived from a 2D analysis that only considers fluid flow in the 2D plane of the beam cross-section. To examine the effect of axial flow, the dimensionless axial flow number, Π_{ax}, is introduced as

$$\Pi_{\text{ax}} = \beta_n b, \tag{51}$$

where b is the beam width, and β_n is the flexural wavenumber. The flexural wavenumber is related to frequency with the expression in Eq. 8, and is also related to the flexural wavelength, λ_n, by

$$\beta_n = \frac{2\pi}{\lambda_n}. \tag{52}$$

Substituting Eq. 52 into Eq. 51, the dimensionless axial flow number may also be expressed as

$$\Pi_{\text{ax}} = 2\pi \frac{b}{\lambda_n}. \tag{53}$$

From Eq. 53, Π_{ax} will generally increase with the increase in bending mode number due to the decrease in corresponding wavelength.

To analyze the effect of axial flow, a numerical parametric study was performed. In the parametric study, beams with doubly-clamped boundary conditions, listed in Table I, were analyzed. In the parametric study, the beams were modeled with no axial load, $P = 0$, resulting in the simplified wavenumber expressed in Eq. 9. An eigenfrequency analysis was then performed to numerically predict the quality factor for the bending mode of interest. The quality factor was also predicted with the blade approximation and Eq. 35. Additionally, with the numerically computed fluid field, the RMS fluid velocity in the x-, y-, and z-direction was computed. The RMS was taken over the fluid volume in the model such that

$$\mathrm{RMS}\{v_i\} = \sqrt{\frac{1}{V}\int ||v_i||^2 dV}, \tag{54}$$

where V is the volume of the fluid field in the FEM. The dimensions of the beam were chosen to give a desired dimensionless axial flow number, as shown in Table I. In the parametric study, the beams were modeled to be in air at atmospheric pressure and temperature $T = 293$ K. The generalized Knudsen number for each beam is listed in Table I. From the reported $\mathrm{Kn}_l + \mathrm{Wi}$, most of the simulations are in the continuum regime with a few remaining in the transition regime. Regardless, for the present parametric study, a no-slip boundary condition is applied and all the systems are approximated to be in the viscous limit. To more accurately asses axial flow results in the continuum regime, numerical results for a simulation in water are presented later in this section.

Results from the parametric study in Fig. 10 depict the fluid field's dependence on the dimensionless axial flow number, Π_{ax}. Figure 10a plots the fluid field in the $x-z$ plane, where color is the real part of the fluid velocity in the x-direction, $\mathrm{Re}\{v_{x,f}\}$, normalized to the real part of the beam velocity in the z-direction at the reference position, $\hat{x}_n$. Here the reference positions for the first three modes are taken to be $\hat{x}_1 = 0.50L$, $\hat{x}_2 = 0.29L$, and $\hat{x}_3 = 0.21L$. The results in Fig. 10a depict an increase in axial flow along the beam with increase in Π_{ax}, evident by the increase in the normalized x fluid velocity. This is also illustrated in Fig. 10b, which plots the normalized RMS fluid velocity in the x-, y-, and z-direction, computed from Eq. 54. Here, the RMS velocity components are normalized to the sum of the RMS components, $\mathrm{RMS}\{v_{x,f}\} + \mathrm{RMS}\{v_{y,f}\} + \mathrm{RMS}\{v_{z,f}\}$. The results are plotted for all beams listed in Table I. From Fig. 10b, it is observed that an increase in Π_{ax} gives rise to a relative increase in $\mathrm{RMS}\{v_{x,f}\}$. Additionally, it is observed that for a fixed Π_{ax}, the normalized RMS velocity components vary with mode number. This is because the 3D fluid field is largely dependent on the shape and response of the beam, as depicted by Fig. 10a.

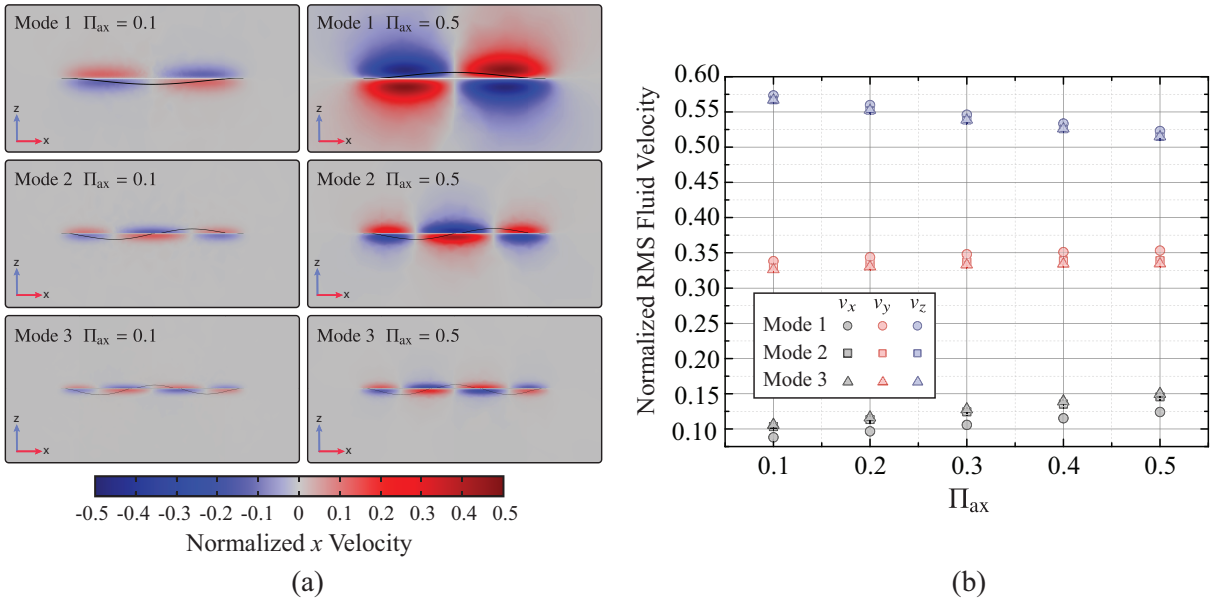

FIG. 10. Results from numerical parametric study for doubly-clamped beams listed in Table I. (a) Fluid field in the $x-z$ plane for various beams. Color represents the real part of the fluid velocity in the x-direction normalized to the real part of the beam velocity in the z-direction at the reference position, $\mathrm{Re}\{v_{x,f}\}/\mathrm{Re}\{\dot{w}(\hat{x}_n)\}$. (b) RMS fluid velocity normalized to the sum of RMS velocity components, $\mathrm{RMS}\{v_{i,f}\} / \left(\Sigma_{j=1}^{3}\mathrm{RMS}\{v_{j,f}\}\right)$,versus dimensionless axial flow number, Π_{ax}, for all beams in Table I.

With an increase in axial flow, the 2D blade approximation over-predicts the dissipative force applied to the beam by the fluid. This is observed in Fig. 11, which plots the inverse of quality factor found from the numerical simulation,

Q_{sim}^{-1}, normalized to the inverse of quality factor predicted from the blade approximation, Q_{rect}^{-1}. From Fig. 11, the blade approximation over-predicts the dissipation at larger Π_{ax}, evident by the decrease in $Q_{\text{sim}}^{-1}/Q_{\text{rect}}^{-1}$ with increase in Π_{ax}. This is due to the increase in axial flow at larger Π_{ax}, which is not accounted for in the 2D blade approximation. When the fluid is allowed to flow in all three directions, such that it is not constrained to the 2D $y-z$ plane, the stress acting on the beam decreases. As a result the fluid load applied to the beam, and the corresponding dissipative force, decreases.

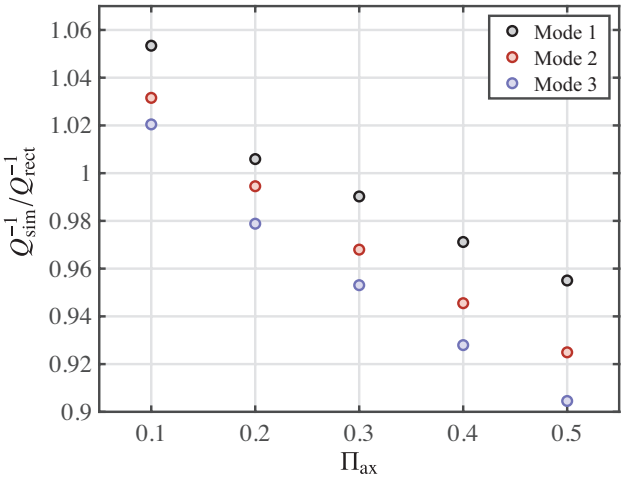

FIG. 11. Results from numerical parametric study for doubly-clamped beams listed in Table I. Inverse of quality factor found from the numerical simulation, Q_{sim}^{-1}, normalized to the inverse of quality factor predicted from the blade approximation, Q_{rect}^{-1} versus dimensionless axial flow number, Π_{ax}.

It is important to note that the quality factor predicted from the numerical simulation is found without any approximation, as the simulation solved the complex eigenvalue problem. Namely, the 3D FEM accounts for fluid loading in all three directions, as expressed in Eq. 4, and the resulting energy dissipated due to such loading. This is in stark contrast to the 2D blade approximation, which only considers fluid loading in the z-direction. The results in Fig. 11 imply that an increase in axial flow results in a decrease in total dissipated energy. In specific, the sum of the energy loss due to loading in the x, y, and z-direction decreases with increasing dimensionless axial flow number, Π_{ax}. Consequently, although the increase in axial flow results in larger velocity gradients in the x-direction, and therefore increased loading in the x-direction, by virtue of Eqs. 3 and 4, the results tend to be dominated by the decrease in loading in the z-direction.

Effects of axial flow were also observed with a simulation of a micro-cantilever vibrating in water. The micro-cantilever had dimensions $L \times b \times h \approx 200\ \mu\text{m} \times 10\ \mu\text{m} \times 1\ \mu\text{m}$. In the simulation, the micro-cantilever was excited with a sinusoidal force applied at the tip of the cantilever. Frequency was then swept to excite the first five bending modes. The receptnace, absolute value of displacement normalized to the applied force at the tip of the cantilever, was computed and is plotted in Fig. 12a. The vertical lines indicate the approximate resonance frequencies where receptance is at a local maximum. The hydrodynamic function was also computed from the simulation with Eq. 43 and is plotted in Fig. 12b. Here, the hydrodynamic function computed from the simulation is compared to that predicted with the blade approximation. In contrast to the blade approximation, which predicts a monotonic decrease in Γ with frequency, the simulation illustrates the hydrodynamic function's dependence on the cantilever's mode shape. Specifically, local minima in Γ'_{sim} and Γ''_{sim} are observed near the resonance of higher modes. The decrease in Γ near resonance is due to the corresponding increase in axial flow near resonance. These trends may be better interpretted by observing the normalized RMS fluid velocity components plotted in the inset of Fig. 6b. Here, two trends may be observed. First, the RMS fluid velocity in the x-direction tends to increase with frequency after the first mode. This is due to the decrease in flexural wavelength and corresponding increase in dimensionless squeeze number, which, as shown previously in Fig. 10b, results in an increase in axial flow. Note that the axial flow number increases from $\Pi_{\text{ax}} = 0.0937$ at the first mode, to $\Pi_{\text{ax}} = 0.7069$ at the fifth mode. The second trend is the local increase in axial flow near resonance. These results suggest that the fluid field, and consequently the hydrodynamic function, is largely dependent on the mode shape and displacement profile of the cantilever. Curvature in the beam gives rise to increase fluid flow in the x-direction and the decrease in fluid loading the the z-direction.

From the results of the two numerical studies, the cylinder and blade approximation become inaccurate and must be modified in the presence of axial flow. Axial flow tends to increase with an increase in dimensionless axial flow

TABLE I. Dimensions and properties of numerically simulated doubly-clamped beams analyzed in parametric study.

		Mode 1				
$\Pi_{\text{ax}} = \beta b$	$b \times h \times l$ (μm^3)	β_1 (μm^{-1})	$\omega_1/2\pi$ (kHz)	$\text{Kn}_l + \text{Wi}$	$\text{Re}(\omega_1, b)$	$\text{Re}(\omega_1, \lambda)$
0.1	$2.11 \times 0.5 \times 100$	0.0473	433.4016	0.0293	0.2020	797.53
0.2	$4.26 \times 0.5 \times 100$	0.0473	433.4016	0.0160	0.8081	797.53
0.3	$6.34 \times 0.5 \times 100$	0.0473	433.4016	0.0116	1.8181	797.53
0.4	$8.46 \times 0.5 \times 100$	0.0473	433.4016	0.0094	3.2323	797.53
0.5	$10.57 \times 0.5 \times 100$	0.0473	433.4016	0.0080	5.0504	797.53
		Mode 2				
$\Pi_{\text{ax}} = \beta b$	$b \times h \times l$ (μm^3)	β_2 (μm^{-1})	$\omega_2/2\pi$ (kHz)	$\text{Kn}_l + \text{Wi}$	$\text{Re}(\omega_2, b)$	$\text{Re}(\omega_2, \lambda)$
0.1	$2.55 \times 0.5 \times 200$	0.0393	298.6769	0.0239	0.2020	797.53
0.2	$5.09 \times 0.5 \times 200$	0.0393	298.6769	0.0129	0.8081	797.53
0.3	$7.64 \times 0.5 \times 200$	0.0393	298.6769	0.0092	1.8181	797.53
0.4	$10.19 \times 0.5 \times 200$	0.0393	298.6769	0.0074	3.2323	797.53
0.5	$12.73 \times 0.5 \times 200$	0.0393	298.6769	0.0063	5.0504	797.53
		Mode 3				
$\Pi_{\text{ax}} = \beta b$	$b \times h \times l$ (μm^3)	β_3 (μm^{-1})	$\omega_3/2\pi$ (kHz)	$\text{Kn}_l + \text{Wi}$	$\text{Re}(\omega_3, b)$	$\text{Re}(\omega_3, \lambda)$
0.1	$4.55 \times 0.5 \times 500$	0.0220	93.6841	0.0129	0.2020	797.53
0.2	$9.09 \times 0.5 \times 500$	0.0220	93.6841	0.0068	0.8081	797.53
0.3	$13.64 \times 0.5 \times 500$	0.0220	93.6841	0.0047	1.8181	797.53
0.4	$18.19 \times 0.5 \times 500$	0.0220	93.6841	0.0037	3.2323	797.53
0.5	$22.74 \times 0.5 \times 500$	0.0220	93.6841	0.0031	5.0504	797.53

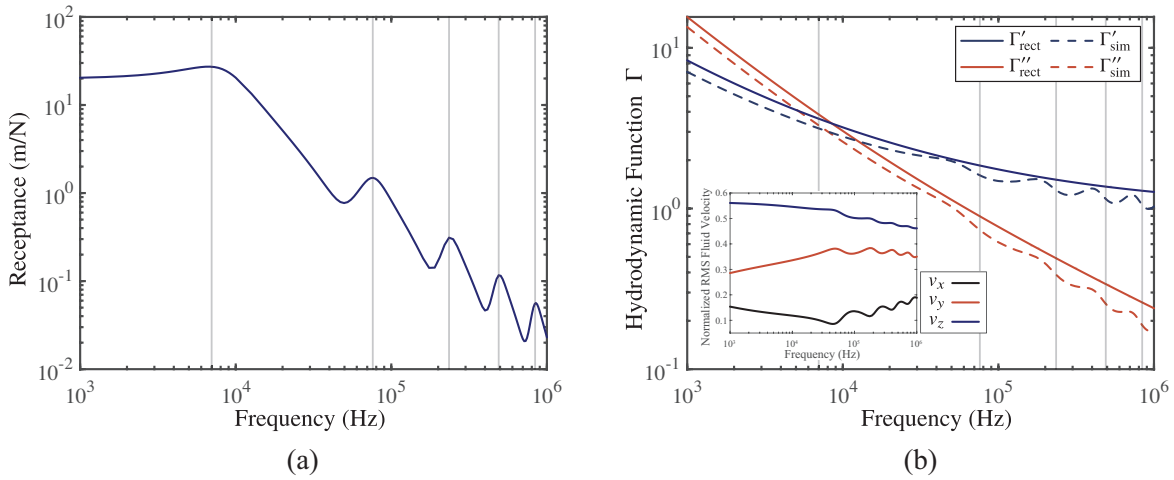

FIG. 12. Results from simulation of micro-cantilever vibrating in water. (a) Receptance, absolute value of displacement normalized to the applied force at the tip of the cantilever, versus frequency. (b) Real, $\Gamma'(\omega)$, and imaginary, $\Gamma''(\omega)$, part of hydrodynamic function versus frequency for blade approximation and simulation. Inset plots RMS fluid velocity normalized to the sum of RMS velocity components, $\text{RMS}\{v_{i,f}\} / \left(\Sigma_{j=1}^{3} \text{RMS}\{v_{j,f}\}\right)$.

number, which is dependent on both the geometry of the beam and flexural wavelength. Furthermore, local increases in axial flow occur near resonance due to the fluid fields strong coupling to the beam's displacement profile. Increase in axial flow results in the corresponding decrease in loading in the z-direction and thus a decrease in the hydrodynamic function. Such trends are not captured in the cylinder or blade approximation which is formulated from a 2D model that only considers planar oscillation of a solid cross-section. Results from Fig. 11 show that errors less than 10% are obtained when $\Pi_{\text{ax}} < 0.5$. However, additional detailed parametric studies are needed to determine exact ranges on Π_{ax} where 3D fluid flow may be neglected. In general, axial flow becomes more prominent at higher bending modes, where the increased curvature of the beam increases the flow in the x-direction. Consequently, neglecting axial flow will produce smaller errors at lower bending modes and smaller values of Π_{ax}.

VII. CONCLUSION

Analyses of 3D nanoflows induced by the vibration of NEMS beams is conducted, and the validity of the 2D cylinder approximation is examined. A dimensionless squeeze number is introduced to characterize the effect of squeeze film damping when a substrate is present. The fluid force applied to a resonator increases with an increase in dimensionless squeeze number, and the 2D cylinder approximation under-predicts the total dissipation due to fluid loading. The effect of the substrate and squeeze film damping is prominent at lower frequencies, where the viscous boundary layer thickness is comparable to the gap distance. In contrast, when the viscous boundary layer thickness is small compared to the gap distance, the substrate does not effect the fluid field and the 2D cylinder approximation is valid. In the present work, evaluation of a 3D FEM coupled with modal analysis allowed for the fluid loading to be analyzed in detail. As previous works have mostly been limited to analyzing the change in quality factor and subsequent change in the imaginary part of the hydrodynamic function, the present work offers new insight into the real part of the fluid loading and hydrodynamic function. Results showed a decrease in the real part of the hydrodynamic function when a substrate was present. From the derived expression of the dynamic stiffness, this decrease is attributed to a decrease in a combined stiffness and mass term. Additional studies may be performed in the future to determine the exact contribution of the individual terms.

A dimensionless axial flow number is also introduced to characterize the resonator and fluid velocity field. The dimensionless squeeze number increases with mode number, as the flexural wave length decreases. When the dimensionless axial flow number increases, the velocity along the axis of the beam increases. Although this gives rise to an increase in fluid loading in the x-direction, the dominant effect is the decrease in loading in the z-direction, resulting in a decrease in total dissipated energy and consequent increase in quality factor. The numerical parametric study analyzed a variety of beams with the dimensionless axial flow number ranging from $\Pi_{\text{ax}} = 0.1$ to $\Pi_{\text{ax}} = 0.5$. This study provided new insight into the effect of axial flow as it isolated the effect of the dimensionless axial flow number and bending mode number. Results show that at a fixed mode number, an increase in dimensionless axial flow number increases the fluid velocity in the x-direction and decreases the quality factor. Additionally, for a fixed dimensionless axial flow number, increasing the mode number will have the identical effect, as the spatial response of the beam is found to effect the flow field.

VIII. ACKNOWLEDGEMENT

This material is based on the work supported by the National Science Foundation Graduate Research Fellowship Program (Grant No. DGE-1840990). Partial support from the National Science Foundation (Grant Nos. CBET-1604075 and CMMI-2001403) is also acknowledged. Any opinions, findings, and conclusions or recommendations expressed in this material are those of the authors and do not necessarily reflect the views of the National Science Foundation.

Appendix A: Governing Equations and Boundary Conditions

Here, the governing equations solved in the FEM are presented. Recalling the FEM depicted in Fig. 2a, the fluid in the the sphere of radius R_1 is modeled as a viscous compressible Newtonian fluid. The fluid is modeled with the following governing equations in the frequency domain: the momentum equation

$$i\omega\rho_0\mathbf{v} = \nabla\cdot\left(-p\mathbf{I} + \mu\left(\nabla\mathbf{v} + (\nabla\mathbf{v})^T\right) + \left(\mu_B - \frac{2}{3}\mu\right)(\nabla\cdot\mathbf{v})\mathbf{I}\right), \tag{A1}$$

where p is pressure in the fluid, $\mathbf{v}$ is the fluid velocity field, μ is the dynamic viscosity, μ_B is the bulk viscosity, and ρ_0 is the mean background fluid density; the continuity equation

$$i\omega\rho = -\rho_0\left(\nabla\cdot\mathbf{v}\right), \tag{A2}$$

where ρ is the fluid density; the energy conservation equation

$$i\omega\left(\rho_0 C_p T - T_0\alpha_0 p\right) = -\nabla\cdot\left(-\mathrm{k}\nabla T\right) + Q, \tag{A3}$$

where T is temperature in the fluid, T_0 is the mean background temperature in the fluid, C_p is the heat capacity at constant pressure, k is the thermal conductivity, α_0 is the coefficient of thermal expansion, and Q is the heat source; and the linearized equation of state

$$\rho = \rho_0(\beta_T p - \alpha_0 T), \tag{A4}$$

where β_T is the isothermal compressibility. The fluid in the outer spherical layer between R_1 and R_2 is modeled as a compressible lossless fluid and is governed by the Helmholtz equation

$$\nabla^2 p - \frac{\omega^2}{c^2} p = 0, \tag{A5}$$

where c is the speed of sound in the fluid. Here, the subscript f, used to denote fluid quantities in the main text, has been left off to improve readability.

In the FEM, the fluid is coupled to the vibrating beam with kinematic and dynamic boundary conditions discussed in Sec. II, Eqs. 1 and 2 respectively. At the substrate, a wall is modeled such that the normal component of the fluid acceleration and velocity are zero, such that

$$\mathbf{n} \cdot \left(\frac{1}{\rho} \nabla p \right) = 0. \tag{A6}$$

At the outer spherical surface of radius R_2, a spherical wave radiation boundary condition is imposed to model the fluid as an infinite medium. Here, the boundary condition allows an outgoing wave to leave the modeling domain with minimal reflections. For this boundary condition, COMSOL Multiphysics® implements second order expressions developed by Bayliss et al. [42].

Appendix B: Convergence Studies

Here, convergence studies performed on the FEM are presented. First, a mesh refinement study was performed to determine the maximum element size. This maximum element size is prescribed to the boundaries at which the fluid and structure are coupled together. Decreasing the element size at this boundary decreases the element size in the fluid domain near the beam. In this region, a fine mesh is needed to capture the losses in the boundary layer. In the mesh refinement study, a mesh factor is set. The mesh factor is related to the maximum element size and viscous boundary layer thickness by

$$\text{maximum element size} = \delta_{\text{visc}}/(\text{mesh factor}). \tag{B1}$$

With the mesh factor and maximum element size, the mesh is generated and the FEM is evaluated to compute the quality factor, Q. The refinement study increases the mesh factor, resulting in finer meshes. For each mesh refinement, a normalized change in quality factor is computed with

$$\text{normalized change in quality factor } = \frac{Q_j - Q_{j-1}}{Q_{j-1}}, \tag{B2}$$

where Q_j is the quality factor computed from the j^{th} iteration. The results from a mesh refinement study performed on a doubly-clamped beam vibrating in its first mode in air is presented in Fig. 13a. The results show a decrease in the change in quality factor with increase in mesh factor. For the present work, a normalized change in quality of less than 1% was desired, and therefore a mesh factor of 3 or greater was used for all FEM.

Additional convergence studies were performed to determine the FEM's sensitivity to the fluid domain size. Specifically, the quality factor's dependence on the spherical radii R_1 and R_2, depicted in Fig. 2, were analyzed in three studies. For the three studies, a doubly-clamped beam vibrating in its first mode in air was studied. The studies performed the following analyses:

Study 1: Computed quality factor for varying R_1 while keeping $\Delta R = R_2 - R_1$ constant.

Study 2: Computed quality factor for varying R_1 while keeping R_2 constant.

Study 3: Computed quality factor for varying R_2 while keeping R_1 constant.

The results from the three studies are presented in Fig. 13b. Here, it is found that changes in the fluid domain size result in relatively small changes in the quality factor. For studies 1, 2, and 3, the difference between the maximum and minimum computed quality factor, normalized to the average compute quality factor is 2.6551×10^{-4}, 5.3914×10^{-4}, and 1.0214×10^{-4} respectively. These results suggest that the computed quality factor is independent of radii R_1 and R_2. The observed insensitivity to domain size is largely due to the fact that the analyzed fluid domain is large compared to the viscous boundary layer thickness, and the fluid is approximately quiescent at R_1.

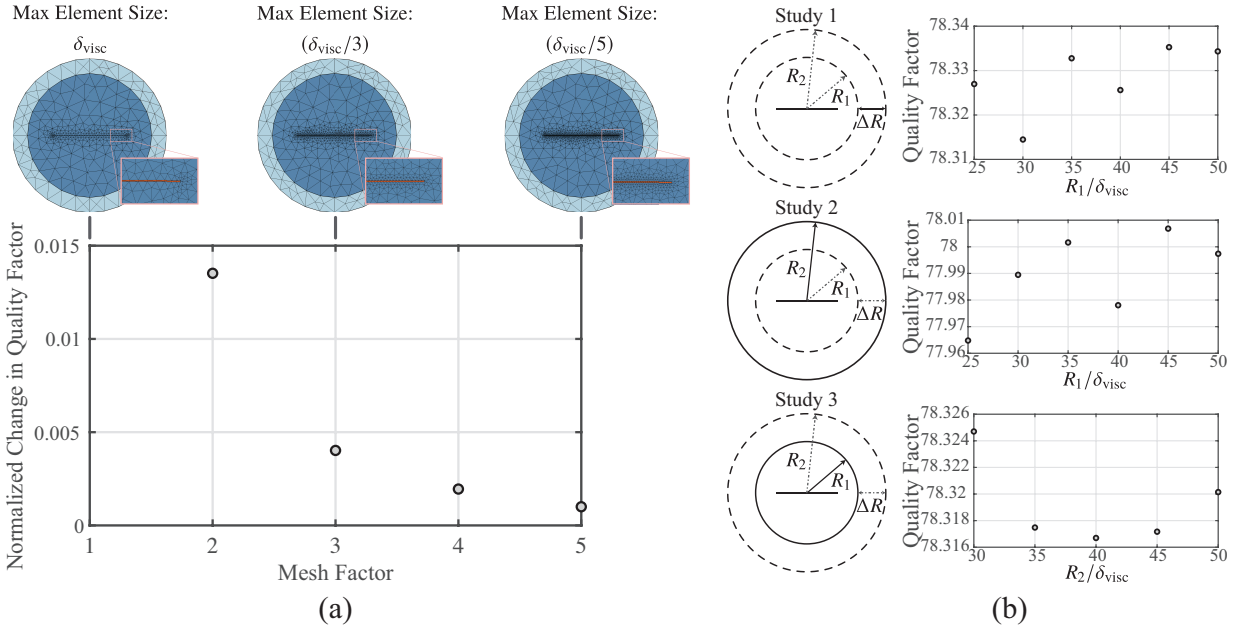

FIG. 13. (a)Normalized change in quality factor, $(Q_j - Q_{j-1})/Q_{j-1}$, versus mesh factor found from mesh refinement study. (b) Results from Study 1-3 of convergence study that analyzed FEM's dependence on fluid domain size. Results plot computed quality factor, Q, versus normalized radius length.

[1] K. L. Ekinci, X. M. H. Huang, and M. L. Roukes, Ultrasensitive nanoelectromechanical mass detection, Applied Physics Letters **84**, 4469 (2004), https://doi.org/10.1063/1.1755417.

[2] J. Tamayo, P. M. Kosaka, J. Ruz, Á. San Paulo, and M. Calleja, Biosensors based on nanomechanical systems, Chemical Society Reviews **42**, 1287 (2013).

[3] C. Lissandrello, F. Inci, M. Francom, M. R. Paul, U. Demirci, and K. L. Ekinci, Nanomechanical motion of escherichia coli adhered to a surface, *Applied Physics Letters*, Applied Physics Letters **105**, 113701 (2014).

[4] V. Yakhot and C. Colosqui, Stokes' second flow problem in a high-frequency limit: application to nanomechanical resonators, *Journal of Fluid Mechanics*, **586**, 249 (2007).

[5] K. L. Ekinci, V. Yakhot, S. Rajauria, C. Colosqui, and D. M. Karabacak, High-frequency nanofluidics: a universal formulation of the fluid dynamics of mems and nems, Lab on a Chip **10**, 3013 (2010).

[6] V. Kara, V. Yakhot, and K. L. Ekinci, Generalized knudsen number for unsteady fluid flow, Physical Review Letters **118**, 074505 (2017).

[7] J. E. Sader, Frequency response of cantilever beams immersed in viscous fluids with applications to the atomic force microscope, *Journal of Applied Physics*, Journal of Applied Physics **84**, 64 (1998).

[8] M. R. Paul, M. T. Clark, and M. C. Cross, The stochastic dynamics of micron and nanoscale elastic cantilevers in fluid: fluctuations from dissipation, *Nanotechnology*, **17**, 4502 (2006).

[9] T. Veijola, H. Kuisma, and J. Lahdenperä, The influence of gas-surface interaction on gas-film damping in a silicon accelerometer, Sensors and Actuators A: Physical **66**, 83 (1998).

[10] M. Bao and H. Yang, Squeeze film air damping in mems, *25th Anniversary of Sensors and Actuators A: Physical*, Sensors and Actuators A: Physical **136**, 3 (2007).

[11] C. Lissandrello, V. Yakhot, and K. L. Ekinci, Crossover from hydrodynamics to the kinetic regime in confined nanoflows, Physical Review Letters **108**, 084501 (2012).

[12] C. D. F. Honig, J. E. Sader, P. Mulvaney, and W. A. Ducker, Lubrication forces in air and accommodation coefficient measured by a thermal damping method using an atomic force microscope, Physical Review E **81**, 056305 (2010).

[13] C. A. Van Eysden and J. E. Sader, Small amplitude oscillations of a flexible thin blade in a viscous fluid: Exact analytical solution, *Physics of Fluids*, Physics of Fluids **18**, 123102 (2006).

[14] F. J. Fahy and P. Gardonio, *Sound and Structural Vibration* (Academic Press, 2007).

[15] L. E. Malvern, *Introduction to the Mechanics of a Continuous Medium* (Prentice-Hall, Inc., 1969).

[16] G. G. Stokes, On the effect of the internal friction of fluids on the motion of pendulums, Transactions of the Cambridge Philosophical Society **9**, 8 (1851).

[17] S. S. Chen, M. W. Wambsganss, and J. A. Jendrzejczyk, Added mass and damping of a vibrating rod in confined viscous fluids, Journal of Applied Mechanics **43**, 325 (1976).

[18] S. S. Rao, *Mechanical Vibrations* (Pearson, 2010).

[19] A. Bokaian, Natural frequencies of beams under tensile axial loads, Journal of Sound and Vibration **142**, 481 (1990).

[20] J. Ginsberg, *Mechanical and Structural Vibrations: Theory and Applications* (Wiley, 2001).

[21] M. Bao, *Analysis and Design Principles of MEMS Devices* (Elsiver Science, 2005).

[22] L. Meirovitch, *Principles and Techniques of Vibrations* (Prentice-Hall, 1997).

[23] K. L. Ekinci, D. M. Karabacak, and V. Yakhot, Universality in oscillating flows, Physical Review Letters **101**, 264501 (2008).

[24] C. M. Harris and C. E. Crede, *Shock and Vibration Handbook* (McGraw-Hill, 1988).

[25] L. Rosenhead, *Laminar Boundary Layers* (Claredon Press, Oxford, 1963).

[26] M. T. Clark, J. E. Sader, J. P. Cleveland, and M. R. Paul, Spectral properties of microcantilevers in viscous fluid, Physical Review E **81**, 046306 (2010).

[27] D. R. Brumley, M. Willcox, and J. E. Sader, Oscillation of cylinders of rectangular cross section immersed in fluid, *Physics of Fluids*, Physics of Fluids **22**, 052001 (2010).

[28] A. Maali, C. Hurth, R. Boisgard, C. Jai, T. Cohen-Bouhacina, and J.-P. Aimé, Hydrodynamics of oscillating atomic force microscopy cantilevers in viscous fluids, *Journal of Applied Physics*, Journal of Applied Physics **97**, 074907 (2005).

[29] A. B. Ari, M. Cagatay Karakan, C. Yanik, I. I. Kaya, and M. Selim Hanay, Intermodal coupling as a probe for detecting nanomechanical modes, Physical Review Applied **9**, 034024 (2018).

[30] I. Bargatin, I. Kozinsky, and M. L. Roukes, Efficient electrothermal actuation of multiple modes of high-frequency nanoelectromechanical resonators, *Applied Physics Letters*, Applied Physics Letters **90**, 093116 (2007).

[31] V. Kara, Y. I. Sohn, H. Atikian, V. Yakhot, M. Lončar, and K. L. Ekinci, Nanofluidics of single-crystal diamond nanomechanical resonators, *Nano Letters*, Nano Letters **15**, 8070 (2015).

[32] M. Gad-el Hak, The fluid mechanics of microdevices—the freeman scholar lecture, Journal of Fluids Engineering **121**, 5 (1999).

[33] E. Lauga, M. Brenner, and H. Stone, Microfluidics: The no-slip boundary condition, in *Springer Handbook of Experimental Fluid Mechanics*, edited by C. Tropea, A. L. Yarin, and J. F. Foss (Springer Berlin Heidelberg, Berlin, Heidelberg, 2007) pp. 1219–1240.

[34] D. M. Karabacak, V. Yakhot, and K. L. Ekinci, High-frequency nanofluidics: An experimental study using nanomechanical resonators, Physical Review Letters **98**, 254505 (2007).

[35] A. B. Ari, M. S. Hanay, M. R. Paul, and K. L. Ekinci, Nanomechanical measurement of the brownian force noise in a

viscous liquid, *Nano Letters*, Nano Letters 10.1021/acs.nanolett.0c03766 (2020).
[36] A. T. Liem, A. B. Ari, J. G. McDaniel, and K. L. Ekinci, An inverse method to predict nems beam properties from natural frequencies, Journal of Applied Mechanics **87**, 10.1115/1.4046445 (2020).
[37] R. Huszank, L. Csedreki, Z. Kertész, and Z. Török, Determination of the density of silicon–nitride thin films by ion-beam analytical techniques (rbs, pixe, stim), Journal of Radioanalytical and Nuclear Chemistry **307**, 341 (2016).
[38] S. D. Senturia, *Microsystem Design* (Springer US, 2001).
[39] C. J. Drummond and T. J. Senden, Characterisation of the mechanical properties of thin film cantilevers with the atomic force microscope, Materials Science Forum **189-190**, 107 (1995).
[40] COMSOL Multiphysics® v. 5.4. www.comsol.com. COMSOL AB, Stockholm, Sweden.
[41] G. K. Batchelor, *An Introduction to Fluid Dynamics* (Cambridge University Press, 2000).
[42] A. Bayliss, M. Gunzburger, and E. Turkel, Boundary conditions for the numerical solution of elliptic equations in exterior regions, *SIAM Journal on Applied Mathematics*, **42**, 430 (1982).